Constraining the ephemeris and interior structure of Io using space-based astrometry by JUICE

Zenk, Kai; Dirkx, Dominic; Fayolle, Sam

DOI
10.1016/j.pss.2025.106112

Publication date
2025

Document Version
Final published version

Published in
Planetary and Space Science

Citation (APA)
Zenk, K., Dirkx, D., & Fayolle, S. (2025). Constraining the ephemeris and interior structure of Io using space-based astrometry by JUICE. *Planetary and Space Science*, *261*, Article 106112. https://doi.org/10.1016/j.pss.2025.106112

Planetary and Space Science 261 (2025) 106112

Contents lists available at ScienceDirect

Planetary and Space Science

journal homepage: www.elsevier.com/locate/pss

Constraining the ephemeris and interior structure of Io using space-based astrometry by JUICE

Kai Zenk [a], Dominic Dirkx [a,*], Sam Fayolle [b,a]

[a] Delft University of Technology, Kluyverweg 1, 2629HS Delft, The Netherlands
[b] European Space Research and Technology Centre, ESA, Keplerlaan 1, 2201AZ Noordwijk, The Netherlands

ARTICLE INFO

Dataset link: https://github.com/kgzenk/juice_space_based_astrometry

Keywords:
Astrometry
Centre-of-figure
Ephemerides
Planets and satellites
Galilean moons
Methods
Data analysis

ABSTRACT

Being among the most promising candidates for potential extraterrestrial habitats within our Solar System, the Galilean satellites are going to be extensively studied by the upcoming JUICE and Europa Clipper missions. Both spacecraft will provide radio science tracking data, which will allow the satellites ephemerides to be determined to much greater accuracy than is currently the case. Yet, with no flybys of Io, these data sets will be skewed towards the three outer satellites. To mitigate this imbalance, optical space-based astrometry from JUICE will provide a valuable contribution.

To quantify the contribution of JUICE astrometry, we have performed the inversion of simulated optical astrometric observations by JUICE, using suitable *a priori* covariance to represent the radio science-only solution. Incorporating the astrometry into the ephemeris solution requires the consideration of the offset between Io's centre-of-figure (COF, which astrometry measures) and the centre-of-mass (COM, which the ephemeris solution requires). We explicitly account for the offset between COF and COM as an estimated parameter in our model.

We assess the contribution of the optical observations to the ephemeris solution as a function of the radio science true-to-formal-error ratio (describing the statistical realism of the simulated radio science solution), as well as optical data quantity and planning. From this, we discuss to which extent space-based astrometry could help to validate the radio science solution, and under which conditions the data could improve the orbital solution of Io.

Significant contributions of astrometry to Io's orbital solution occur for radio science true-to-formal-error ratios of 4 and higher (for the along-track and normal direction). This shows that optical space-based astrometry can improve and/or validate the radio science solution. Reductions in the obtainable uncertainties for the COF-COM-offset range from about 20 to 50 per cent – depending on the number of observations – using suitable algorithms to select the epochs at which observations are to be simulated. In particular, observations during the high-inclination phase have proven especially beneficial.

Our results show that constraints on the COM-COF offset of Io could be obtained from astrometry at the level 100 m – 1 km, depending on the quantity and planning of the observations. This could provide a novel data point to constrain Io's interior. Moreover, the astrometric data will provide independent validation – and possibly improvement – of the orbital solution of Io.

1. Introduction

The Galilean satellites are among the most promising candidates for potential extraterrestrial habitats within our Solar System. To investigate the general existence and stability of these presumed habitable worlds – in particular, the presence of sub-surface oceans – as well as to shed light on the formation of the entire Solar System, understanding the evolution of these moons is crucial (*e.g.* Fuller et al., 2016; Heller et al., 2015; Samuel et al., 2019). In particular, tidal dissipation and heating – estimable by meticulously reconstructing the dynamics of the Galilean satellites – are key to the orbital evolution of planetary systems (Dirkx et al., 2017; Greenberg, 2010; Schubert et al., 2004). Hence, the significant tidal coupling between Jupiter and Io – with the latter being the most volcanically active object in the Solar System due to tidally induced heating (*e.g.* Davies, 2007; Peale et al., 1979) – distinctively drives the long-term evolution of the Jovian

* Corresponding author.
E-mail address: d.dirkx@tudelft.nl (D. Dirkx).

https://doi.org/10.1016/j.pss.2025.106112
Received 31 October 2024; Received in revised form 24 March 2025; Accepted 2 April 2025
Available online 8 April 2025

system. Yet, given the complex dynamics of the Galilean satellites due to the one-two-four mean motion Laplace resonance between Io, Europa, and Ganymede (*e.g.* Lainey et al., 2006; Lari, 2018), improved ephemerides' solutions are necessary to detect the secular signatures of tidal mechanisms (Greenberg, 2010; Lainey et al., 2004, 2009, 2012).

To date, ephemeris solutions for the Galilean moons are mainly based on optical ground-based astrometric observations spanning a period of more than a century, irregularly supplemented by space-based astrometric images and tracking data from Voyager and Galileo (Lainey et al., 2004, 2009; Lieske, 1998; Jacobson et al., 2000). Even though classical ground-based astrometric observations are indispensable to reconstruct the long-term orbital dynamics of the Jovian system (*e.g.* Vienne, 2008; Lainey et al., 2009; Dias-Oliveira et al., 2013), the determination of extremely weak dynamical effects (such as tidal dissipation) requires significantly more accurate measurements of the states of the Galilean satellites (Fayolle et al., 2021). Thus, radio science tracking data of both ESA's upcoming JUICE and NASA's Europa Clipper missions will provide highly accurate – yet indirect – constraints, anticipated to yield pivotal insights into the dynamics of the Galilean satellites (*e.g.* Fayolle et al., 2023).

However, while the dynamics of Ganymede (in particular via the orbital phase of JUICE) and Europa (mainly via the various flybys of Europa Clipper) are going to be observed to an unprecedented level of accuracy (Cappuccio et al., 2020; Fayolle et al., 2022; Magnanini et al., 2024), the absence of flybys of Io due to its harsh radiation-environment results in a significantly skewed data set. Even though we expect significant improvements as a result of the global inversion of existing ground-based astrometric observations (Fayolle et al., 2023), the combined radio science solution by JUICE and Europa Clipper is going to greatly dominate the estimation of the moons' ephemerides over the time spans of the missions. With the state of Io only indirectly constrained via the Laplace resonance, the correlations between the respective moons' states render the reconstruction of the satellites' dynamics unstable, while simultaneously leading to a rapid increase in the propagated uncertainties of Io outside of the missions' time spans. To stabilise the estimation of Io's ephemeris solution, merging the radio science data from JUICE and Europa Clipper with optical space-based astrometry by the imaging subsystem of JUICE has been suggested to constrain the dynamics of Io (*e.g.* Dirkx et al., 2017; Fayolle et al., 2022), as it has previously been done for the Saturnian satellites using optical data taken by Cassini (Lainey et al., 2012, 2017, 2020).

In general, space-based imaging of natural satellites has become increasingly popular within the field of astrometry. Recent applications include observations of Saturn's satellites by the Hubble Space Telescope (French et al., 2006), astrometry performed on images of the Martian satellites Deimos and Phobos taken by the Mars Express mission (Oberst et al., 2006; Willner et al., 2008; Pasewaldt et al., 2012), as well as reductions of observations taken by Cassini of both Amalthea and Thebe (Cooper et al., 2006), and a series of Saturnian satellites (Tajeddine et al., 2013, 2015). Furthermore, owing to the relative proximity of space-based observers, space-based astrometric observations yield an unparalleled level of accuracy – compared to classical astrometry and the observation of mutual phenomena from Earth – in the order of a mere few kilometres (Tajeddine et al., 2013, 2015). Besides their low level of formal uncertainties, the different observation geometries compared to ground-based observations and the independence of Jupiter's opposition make space-based astrometry highly interesting (*e.g.* Fayolle et al., 2023). Overall, space-based imaging has proven essential in the accurate determination of ephemerides (Gomes-Júnior et al., 2022; Tajeddine et al., 2015).

However, while the inversion of orbital dynamics is usually performed with respect to the centre-of-mass (COM) of natural satellites, optical space-based astrometry yields the position of a body's centre-of-figure (COF) in an absolute reference frame (*e.g.* Pasewaldt et al., 2012). For most natural satellites – with the Moon being a prominent exception (Smith et al., 1997; Zuber et al., 1994) – a quantification for the offset between the respective centre-of-mass and centre-of-figure is lacking. Nevertheless, given the high expected accuracy of space-based astrometry – up to one kilometre at times for Cassini (Tajeddine et al., 2015) – already small offsets could potentially be one of the most dominant – but so far unaccounted – sources of error in the astrometric reduction of space-based optical data of Io. Thus, even though the combined tracking data of JUICE and Europa Clipper, as well as expected future improvements due to global inversion strategies will already significantly enhance and balance the orbital solution of Io (Fayolle et al., 2023), the realistic reduction of space-based astrometry is crucial to stabilise the data inversion. Furthermore, optical observations will yield an independent data set which might prove beneficial to validate the radio science solution of Io in particular. This is conceptually similar to one of the roles of the Very Long Baseline Interferometry (VLBI) data of JUICE described by Fayolle et al. (2024). Although the VLBI data will provide stronger linear constraints/validation than the optical astrometry, the strength of the optical data lies in providing direct information on Io, which is not accessible by spacecraft tracking.

Obtaining a measure of the offset between the centre-of-figure and centre-of-mass of Io furthermore yields an entirely new constraint on the physical state of Io, potentially allowing us to draw conclusions on the melt fraction of Io's mantle or variations in crustal thickness and asymmetry in its internal composition. Exploiting the tidal coupling between Io and Jupiter, this could, in turn, lead to an improvement in our understanding of how tidal dissipation, melting, and heat transport interact (Steinke, 2021). To date, the interior structure and composition of Io remain highly debated. Even though various types of observations constrain the moon's interior, they are usually a sufficient but not necessary condition, leading to a – sometimes even contradicting – intricate chain of logical arguments to which the offset between the COF and COM will add a new link. Nonetheless, it is crucial to find a consistent description of Io's internal structure that is in line with all available observations and physical and chemical laws (Steinke, 2021). As of yet, constraints of the interior of Io have thus mainly been based on inferences drawn from measurements of both the gravity (*e.g.* Anderson et al., 2001; Moore et al., 2007) and magnetic field (Khurana et al., 2011), as well as observations of the topography (Thomas et al., 1998), the ubiquitous volcanoes (Keszthelyi et al., 2007; Davies et al., 2023), or the oscillation of auroral spots (Roth et al., 2017).

To improve the quality of the orbital solution of Io using optical space-based astrometry and constrain the offset between the centre-of-figure and centre-of-mass, this paper develops an estimation framework to account for a potential discrepancy between the imaged centre-of-figure and propagated centre-of-mass of Io. To this end, space-based astrometric observations taken by the NavCam of JUICE are simulated. In contrast to mimicking images using JANUS, the camera of the science payload – having a slightly higher resolution – the chosen approach yields a conservative baseline in terms of the astrometric reduction. Yet, we want to stress that at present, owing to the absence of flybys, the baseline operations of the NavCam do not include any observations of Io. JANUS, on the other hand, will exploit a few observation opportunities to study the surface activity and composition of Io, as well as its torus (Palumbo et al., 2025). In contrast to astrometric observations needed for ephemerides refinement purposes, the feasibility criteria for such observations differ significantly in terms of distance to Io and illumination conditions. In particular, monitoring the surface of Io – even at global scales – requires a spatial resolution of a few hundred kilometres per pixel, substantially reducing the number of potential observation opportunities given the current trajectory of JUICE. However, realise that such limitations are irrelevant for images destined to help refine the orbital solution of Io.

To this end, we have simulated space-based astrometric observations of Io using the less strict – and in the context of this work thus more realistic – feasibility criteria of the NavCam. Investigating their potential for ephemerides determination might even motivate the

inclusion of such distant observations of Io in the operations of the navigation camera or optical instruments of JUICE. Owing to the substantial variations in relative observation geometries and formal uncertainties, suitable epoch selection algorithms are implemented and reviewed. Using the results by Fayolle et al. (2023), the estimated formal errors are constrained to the expected level of uncertainties of the combined radio science solution of JUICE and Europa Clipper without having to implement their intricate tracking set-up. Finally, we discuss how the found results could either validate the radio science solution or better constrain the estimated orbital solution and simultaneously shed light on the formation and interior structure of Io.

Analytical models used for the mathematical description and propagation of the Galilean moons' orbital dynamics are first delineated in Section 2, covering gravitational interaction, rotation models, and the computation of tides. Subsequently, Section 3 gives an outline of how space-based optical observations are simulated, followed by a brief overview of the relevant foundations of orbit determination in Section 4 before presenting our results and findings in Section 5. Finally, we discuss the implications of the provided outcomes on the validation of the radio science solution and the estimation of the orbit of the Galilean moons, as well as any arising constraints for the satellite's interior structure, before conclusions can be drawn in Sections 6 and 7, respectively.

2. Orbital dynamics and models

Here, we describe the dynamical models used to propagate the state of the Galilean moons, based on Lainey et al. (2004, 2009), Fayolle et al. (2022). In Section 2.1, we describe the acceleration-model of gravitationally interacting extended bodies. Subsequently, we provide the explicit equations of motion for the satellites in Section 2.2 and summarise relevant physical characteristics of the Jovian system in Section 2.3.

2.1. Gravitational interactions

In general, the gravitational acceleration of an arbitrary body i due to body j can be decomposed into the interactions between two point masses, between one point mass and an extended body, and between two extended bodies (Lainey et al., 2004):

$$\ddot{\vec{r}}_{ij} = \ddot{\vec{r}}_{\bar{i}\bar{j}} + \ddot{\vec{r}}_{\bar{i}\hat{j}} + \ddot{\vec{r}}_{\hat{i}\bar{j}} + \ddot{\vec{r}}_{\hat{i}\hat{j}}, \tag{1}$$

where $\vec{r}_{ij} = \vec{r}_i - \vec{r}_j$ denotes the vector between the centres-of-mass of the two bodies, and indexed bars or hats indicate treatment as a punctual or extended body, respectively. It is common practice to omit the last term delineating – very small – extended body interactions (Lainey et al., 2004), an assumption further justified in the work of Dirkx et al. (2016, 2019). Introducing the gravitational potential functions U_i and U_j of bodies i and j, the remaining terms can be written as

$$\ddot{\vec{r}}_{\bar{i}\bar{j}} = \mu_j \nabla U_{\bar{j}}\left(\vec{r}_{ij}\right), \tag{2a}$$

$$\ddot{\vec{r}}_{\bar{i}\hat{j}} = \mu_j \nabla U_{\hat{j}}\left(\vec{r}_{ij}\right), \tag{2b}$$

$$\ddot{\vec{r}}_{\hat{i}\bar{j}} = -\mu_j \nabla U_{\hat{i}}\left(-\vec{r}_{ij}\right), \tag{2c}$$

where μ_j denotes the gravitational parameter of body j gravitationally interacting with body i. For the explicit expression of the gravitational potentials, we have

$$U_{\bar{j}}\left(\vec{r}_{ij}\right) = \frac{1}{r_{ij}}, \tag{3a}$$

$$U_{\hat{j}}\left(\vec{r}_{ij}\right) = \frac{1}{r_{ij}} \sum_{l=1}^{\infty} \sum_{m=0}^{l} \left(\frac{R_j}{r_{ij}}\right)^l \times P_{lm}\left(\sin(\phi_{ij})\right)\left(C_{lm}^{(j)} \cos(m\lambda_{ij}) + S_{lm}^{(j)} \sin(m\lambda_{ij})\right), \tag{3b}$$

where R_j is the reference radius of the spherical harmonic expansion (usually the equatorial radius of body j), while ϕ_{ij} and λ_{ij} are latitude and longitude of body i with respect to body j, respectively. P_{lm} denotes the so-called associated Legendre polynomial of degree l and order m, and $C_{lm}^{(j)}$ and $S_{lm}^{(j)}$ are the spherical harmonic coefficients associated with body j and are a measure of the internal mass distribution. In Section 2.3, these properties are discussed in more detail in the context of the Jovian system.

In our rotation models of the satellites, their long axis always points towards Jupiter (i.e. for Io $\lambda_{(\text{Io, Jupiter})}$ is equal to zero in Eq. (3b)), in line with dynamical models used by *e.g.* Lainey et al. (2004). Qualitatively, a more realistic model, for instance, with the satellite's long axis (almost exactly) pointing towards the orbit's empty focus due to the effect of eccentricity, will result in a small secular drift of the periapsis. For the purposes of our analysis, the absence/presence of such an effect does not alter our conclusions (as verified by numerical experiments). Moreover, adding this term has an almost identical effect on the orbital evolution as a slight variation in the C_{20} and C_{22} gravity field coefficients (Jacobson, 2010).

2.2. Equations of motion

The equations of motions are integrated numerically in a Jovicentric frame with inertial axis orientation (ECLIPJ2000) using the TU Delft Astrodynamics Toolbox (tudat)[1] (Dirkx et al., 2019, 2022). For the Galilean system, our implementation builds on past analyses by Dirkx et al. (2016, 2017), Fayolle et al. (2022, 2023), using the same toolbox as core libraries. The complete expression for the equation of motion for satellite i of mass m_i around a central planet of mass m_0 is given by

$$\begin{aligned}\ddot{\vec{r}}_i = {} & \nabla U_{0i}\left(\vec{r}_i\right) - \nabla U_{i0}\left(-\vec{r}_i\right) + \sum_{j=1, j\neq i}^{N} \nabla U_{ji}\left(\vec{r}_{ji}\right) - \nabla U_{j0}\left(-\vec{r}_j\right) \\ & + \frac{\left(m_0 + m_i\right)}{m_i m_0}\left(\vec{F}_{\bar{i}\hat{0}} - \vec{F}_{\bar{0}i}\right) - \frac{1}{m_0} \sum_{j=1, j\neq i}^{N} \left(\vec{F}_{\bar{j}\hat{0}} - \vec{F}_{\bar{0}\hat{j}}\right),\end{aligned} \tag{4}$$

where $U_{ij}\left(\vec{r}_{ij}\right)$ is the combined gravitational potential (including the respective gravitational parameter) directly obtained from Eqs. (1) and (2), and $\vec{F}_{\bar{i}\bar{j}}$ denotes the respective tidal forces in accordance with the derivation by Lainey et al. (2007, 2009). In particular, when propagating the dynamics of the Galilean satellites using Eq. (4), the following models have been taken into account:

- the mutual spherical harmonic acceleration between Jupiter and each moon, with the gravity field of Jupiter expanded up to degree 12 and order 0, and that of each moon considered up to degree and order 2,
- the mutual spherical harmonic accelerations between all moons with the gravity fields of the bodies expanded up to degree and order 2,
- the point-mass accelerations exerted by both Saturn and the Sun,
- the acceleration exerted on each moon due to tidal dissipation in Jupiter forced by the same moon,
- the acceleration on each moon due to tidal dissipation within the same moon forced by Jupiter.

While propagating the state of the Galilean moons, the trajectory of JUICE is taken from the CReMA 5.1 trajectory,[2] distributed by ESA in the form of SPICE kernels.

[1] Documentation: https://tudat-space.readthedocs.io
Source code: https://github.com/tudat-team/tudat-bundle

[2] https://www.cosmos.esa.int/web/spice/spice-for-juice

2.3. Physical characteristics of the jovian system

For the gravity field coefficients of the Galilean moons, we use the μ, J_2, and C_{22} coefficients of each moon (Schubert et al., 2004), while the other coefficients are kept equal to zero. Concerning the gravity field of Jupiter, the first results of the Juno mission by Iess et al. (2018) were used, while the value for μ has been taken from Folkner et al. (2017). Finally, the tidal properties of the Galilean moons implicitly used in Eqs. (4) are poorly constrained. Solely the characteristics of Io have been determined by Lainey et al. (2009) to $k_2/Q = 0.015 \pm 0.003$, which will also be used for the three remaining moons. In the same astrometry-based analysis, an estimate of $(1.102 \pm 0.203)\cdot10^{-5}$ has been found for Jupiter's value of k_2/Q.

3. Simulation of optical observations

With astrometric observations, the position of an imaged celestial body – right ascension and declination – is determined with respect to an absolute reference frame such as the ICRF (International Celestial Reference Frame). For space-based astrometry (as opposed to ground-based astrometry), the proximity of the target to the observer introduces a number of specific considerations into the data analysis. This section first delineates the dominant sources of uncertainty of optical space-based astrometric observations in Section 3.1. Finally, Section 3.2 outlines the different types of observation epoch selection algorithms that we have developed for our simulations.

3.1. Optical space-based astrometry

An overview of a number of past analyses of space astrometry data for the determination of satellite ephemerides has been presented in the introduction. Three main sources of error constitute the overall uncertainty of space-based astrometric observations (Tajeddine et al., 2013): uncertainties related to determining the centre-of-figure (σ_c), errors in the pointing correction (σ_p), and the positional accuracy of the spacecraft itself (σ_{sc}). First – also taking uncertainties within the shape model into account – σ_c delineates how well the position of the centre-of-figure can be reduced from the detectable limb of the satellite. Second, σ_p accounts for the finite accuracy of the astrometric calibration of the orientation and pointing direction of the camera (Tajeddine et al., 2013). Finally, σ_{sc} describes how the uncertainty in the position of the spacecraft directly propagates into the accuracy of the observation of the moon. Note that the total uncertainty will be mainly dominated by the error within the determination of the centre-of-figure, with σ_p about one and σ_{sc} around two orders of magnitude smaller, respectively (Melman, 2018). For the total observational uncertainty of space-based imaging expressed in right ascension α and declination δ, thus follows (Pasewaldt et al., 2012; Tajeddine et al., 2013):

$$\sigma_\alpha = \sqrt{\left(\sigma_c^2 + \sigma_p^2 + \sigma_{sc}^2\right)} / \cos\delta, \tag{5a}$$

$$\sigma_\delta = \sqrt{\left(\sigma_c^2 + \sigma_p^2 + \sigma_{sc}^2\right)}. \tag{5b}$$

On a final note, the implication of reducing images by JANUS instead of those by the NavCam – as investigated in this work – should be discussed, in the case that the science camera takes more pictures of Io than planned. The quadratic field-of-views and similar resolutions of the navigation camera of JUICE and that of Cassini – in the following used to establish a realistic simulation of the error budget of the NavCam – will yield roughly identical values for the pointing and spacecraft position uncertainties. This does, however, not necessarily hold for the higher resolution and rectangular field-of-view of JANUS, supporting our approach to establish a realistic NavCam error budget. In particular, while JANUS thus theoretically achieves a lower pointing uncertainty, owing to its narrower field-of-view and higher resolution of the detector (scaled by factors of approximately 0.4 and 1.7, respectively) we observe an increase in the apparent diameter and thus the centre-of-figure uncertainty. In a first approximation, these two opposed effects will roughly level each other out. We may thus conclude that the results presented in Section 5 would quantitatively be roughly independent of the respective imaging system. Hence, given the conceptual nature of our work, the overall conclusions would remain unaffected when using images by JANUS instead of the NavCam.

Table 1
Fitted values for the weighting factor σ_{min} and scaling factor C in Eq. (6), as well as the resulting coefficient of determination R^2 for the five Saturnian moons delineated by Tajeddine et al. (2015).

Moon	σ_{min}	C	R^2
Tethys	0.087 ± 0.0011	0.00062 ± 0.00014	0.6345
Dione	0.083 ± 0.0010	0.00052 ± 0.00015	0.6735
Rhea	0.076 ± 0.0011	0.00077 ± 0.00009	0.6293
Iapetus	0.086 ± 0.0012	0.0014 ± 0.00013	0.7964
Phoebe	0.141 ± 0.0051	0.0021 ± 0.0011	0.4582

3.1.1. Centre-of-figure uncertainty

To determine the uncertainty within the determination of the centre-of-figure (i.e. how well a given shape model can be fitted to the detectable limb of a satellite), Antreasian et al. (2005) have developed an expression that gives the uncertainty σ_c as a function of the apparent diameter d_a, and thus the position of the spacecraft with respect to the imaged satellite:

$$\sigma_c^2 = \sigma_{min}^2 + \left(C \cdot d_a\right)^2, \tag{6}$$

where σ_{min} is a fixed weighting factor, and C is a scaling factor related to the moon's surface roughness.

For Cassini, however, Melman (2018) finds poor agreement between the values of σ_{min} and C initially given in Antreasian et al. (2005) and the errors reported in Tajeddine et al. (2015) – based on a novel but not further delineated limb-fitting scheme – with the found analytic expression (Eq. (6)) yielding too pessimistic results (see Appendix). To this end, we have used the obtained uncertainties for the five Saturnian moons' declination by Tajeddine et al. (2015) as provided in the supplementary information.[3] alongside the moons' instantaneous apparent diameter to fit the variable parameters within the model by Antreasian et al. (2005) using a non-linear least-squares algorithm (see Section 4.1). The individual fitted values for the five Saturnian moons analysed by Tajeddine et al. (2015) are presented in Table 1, together with the respective coefficient of determination. An in-depth outline of the fitting process as well as an analysis of the results can be found in the Appendix, which shows good agreement between our model (Eq. (6)) and the results of Tajeddine et al. (2015).

Given that the geometrical specifications of the corresponding field-of-views significantly differ between the imaging subsystems of Cassini and JUICE, we have to scale the limb-fitting uncertainty given by Tajeddine et al. (2015) using a factor of $FOV_{NavCam}/FOV_{NAC} = 4/0.35$ to mimic the results that would have been expected when using a NavCam-like camera instead of Cassini's NAC. Using the averaged parameters given in Table 1, we find values of 0.095 pixels and 0.0014 for σ_{min} and C, respectively – approximately one order of magnitude lower than those originally proposed by Antreasian et al. (2005).

3.1.2. Pointing uncertainty

In practice, the pointing correction of the imaging subsystem is achieved using the catalogued positions of imaged reference stars – such as the Gaia DR2 and EDR3 catalogue (Gaia Collaboration, 2018, 2021). Tajeddine et al. (2013) base their applied reduction technique

[3] http://cdsarc.u-strasbg.fr/viz-bin/qcat?J/A+A/575/A73

on the actual optical properties of space-based images (such as the camera's constant scale factors or errors in a star's position due to the projection of the image from the celestial sphere to the tangential observation plane of the camera). This approach is, however, less suitable for the description of simulated uncertainties, where this information is not necessarily available. As an alternative, Melman (2018) has modelled errors in the pointing correction using a theory for the accuracy of a star tracker by Liebe (1995). Using this model, σ_{p} can be described as a function of the size of the field of view of the camera FOV in degrees, the achievable sub-pixel precision of the stars' position $\sigma_{\mathrm{extraction}}$, and the number of pixels and stars in the field of view, N_{pixels} and N_{FOV}, respectively:

$$\sigma_{\mathrm{p}} = \frac{FOV \cdot \sigma_{\mathrm{extraction}}}{N_{\mathrm{pixels}} \cdot \sqrt{N_{\mathrm{FOV}}}}. \tag{7}$$

For Cassini, Tajeddine et al. (2013) report a value of approximately 0.552 pixels for $\sigma_{\mathrm{extraction}}$, which also seems a reasonable estimate for the imaging subsystem of JUICE, assuming similar data-reduction techniques. Since the pointing uncertainty is a function of the instantaneous number of background stars visible in the field of view (FOV), no absolute *a priori* uncertainty for the pointing correction is readily available. To this end, we assume the number of background stars to be fixed to its average value – estimated to approximately 800 stars by Melman (2018). Whereas Cassini's NAC has observed an average of 6.14 stars per image (Tajeddine et al., 2013, 2015), this seemingly elevated number is in line with a linear scaling by the ratio of the sizes of the respective field-of-views.

3.1.3. Spacecraft position uncertainty

Finally, the overall achievable accuracy in the observed position of the satellite depends on the uncertainties in determining the spacecraft's position. According to Tajeddine et al. (2013), the influence of the spacecraft uncertainty on the uncertainty in the moon's lateral position can be expressed as:

$$\sigma_{sc} = \arcsin\left(\frac{\sigma_{S/C}}{D}\right), \tag{8}$$

where D is the distance between the spacecraft and the satellite, and $\sigma_{S/C}$ is the total uncertainty in the position of the spacecraft. For Cassini, Tajeddine et al. (2013) assume a position uncertainty $\sigma_{S/C}$ of 100 metres. Given the largely comparable tracking equipment of Cassini and JUICE outside of any flyby- or orbital phases, a position uncertainty of 100 metres seems to be a reasonable approximation for the expected accuracy of JUICE, as well. Nonetheless, note that the contribution of the uncertainty in the spacecraft position – about two orders of magnitude smaller than the limb-fitting error (Melman, 2018) – to the overall uncertainty of space-based astrometry is almost entirely negligible.

3.2. Selection of observation epochs

Since both the overall uncertainty and the relative geometry of optical space-based astrometry are a function of the position of JUICE with respect to that of Io – and thus of their respective orbits – the selection of epochs at which we simulate optical observations may have a significant impact on the orbital solution. Moreover, we have to define a set of viability criteria to dismiss any physically implausible observations. These constraints will be briefly delineated in Section 3.2.1. Further, in Section 3.2.2, we propose the implementation of four different algorithms for the selection of the epochs at which optical observations are to be simulated.

3.2.1. Observation schedule and constraints

To date, the current mission design of JUICE stipulates a NavCam observation schedule covering the period from Jupiter Orbit Insertion (July 2031) up to Ganymede Orbit Insertion (December 2034). Within this period, we have chosen a minimum imaging cadence of one observation per 30 minutes. However, from an observational point-of-view, only a limited subset of all potential epochs is considered feasible. No images are taken during the 12 h directly before and after the moment of closest approach of all flybys performed by JUICE (Boutonnet et al., 2018). In addition, the following constraints apply:

- a minimum Sun-Spacecraft-Moon angle,
- a minimum Jupiter-Limb-Spacecraft-Moon angle,
- a maximum Sun-Moon-Spacecraft angle (Phase angle).

By limiting the influence of other celestial bodies' brightness on the saturation of the digital imagining sensor, both the minimum Sun-Spacecraft-Moon and Jupiter-Limb-Spacecraft-Moon angles ensure sufficient visibility of background stars in the camera's FOV. Moreover, since a reasonable part of the visible surface of Io needs to be illuminated by the Sun to avoid erroneous fits of the satellite's limb, as well as to avoid loss of contrast due to imaging into direct sunlight, a maximum phase angle needs to be introduced (Cooper et al., 2014). While the minimum Sun-Spacecraft-Moon angle (30 degrees) and the maximum Sun-Moon-Spacecraft angle (130 degrees) have been fixed to constant values, the minimum Jupiter-Limb-Spacecraft-Moon angle depends on the apparent size of Jupiter. For an imaged size greater than 4 degrees, the minimum Jupiter-Limb-Spacecraft-Moon angle has been set to 5 degrees, while a distance to Jupiter's limb of 10 degrees is required otherwise. Finally, note that any other constraints, such as the minimum number of pixels to be filled by the imaged satellite, were never found to be active in any of our analyses, and we do not reiterate them here.

3.2.2. Epoch selection algorithms

We will present our results in Section 5 as a function of the number of astrometric observations (out of all feasible ones), for which we define four distinct epoch selection algorithms

- a randomised approach,
- a geometry-driven approach,
- an uncertainty-driven approach,
- an uncertainty- and geometry-driven hybrid approach.

Realise that all four algorithms will be evaluated in the context of a rigorous Monte-Carlo analysis (see Section 5). In particular, we will perform 100 runs of each algorithm to obtain different – but equally adequate – possible representations of the selected observation set.

Randomised approach: To give no priority to individual epochs, an entire randomised selection – out of the total feasible subset – takes place when using the randomised approach.

Geometry-driven approach: Different observation geometries are crucial to constrain the offset between a celestial body's COF and COM (Pasewaldt et al., 2012). Since the observation geometry is constrained by the minimum Jupiter-Limb-Spacecraft-Moon angle (see Section 3.2.1) and the mostly equatorial observation geometry of JUICE, the along-track position of Io will be less prominently observed than the radial or normal direction. To diversify the set of chosen observation geometries, we introduce a grid with X nodes (with X being the number of required observations), evenly spread over all possible values of the relative observation angles (i.e. the angle between the observation direction and the along-track axis of Io). The observations are then planned to maximise their uniform distribution over this grid.

Uncertainty-driven approach: Given otherwise similar estimation conditions, more accurate observations (in absolute terms – see Section 3.1), by definition, yield lower estimated formal errors (see Section 4.2). To this end, we propose an uncertainty-driven algorithm

selecting the best X epochs purely based on their expected absolute (i.e. in metres) uncertainty, with the best X equal to the total number of observations. However, owing to the operational constraints of the NavCam – for instance observations of the remaining three moons for navigational purposes – a random selection is performed out of the $1.2X$ most accurate epochs, making our simulations more realistic and lenient in the choice of epochs.

Hybrid approach: Finally, we expect synergistic effects by merging the underlying ideas of the uncertainty and geometry-driven algorithms. This hybrid approach thus still favours the most accurate epochs (as in the uncertainty-driven method), while simultaneously providing a differentiated geometric coverage, and most importantly of the along-track direction (as in the geometry-driven algorithm).

4. Determination of orbits

In this section, we briefly describe how the estimated solution for the orbit of Io is determined from simulated optical space-based astrometric observations. We present the mathematical foundations of 'full' orbit estimation, and covariance analyses in Sections 4.1 and 4.2, respectively. Subsequently, to address our research objective outlined in the introduction, we discuss our choice of approach to model the offset between the COF and COM in Section 4.4. Finally, we discuss how we constrain our analysis to the expected average uncertainty level of the radio science solution using a suitable *a priori* covariance matrix in Section 4.3.

4.1. Orbit estimation

Overall, orbit estimation tries to minimise the residuals between a set of observations $\vec{z}$ and the respective computed values $\vec{h}(\vec{q})$ (i.e. the observables predicted by the propagated equations of motion, see Section 2.2). Using a least-squares algorithm (*e.g.* Montenbruck and Gill, 2000; Milani and Gronchi, 2010), this can mathematically be defined as finding the set of estimated parameters $\vec{q}$ that minimises the weighted residual between the observed and computed observations. The vector $\vec{q}$ usually contains initial states $\vec{x}_0$ and any parameters $\vec{p}$ of interest that influence the dynamical or observational models (i.e. $\vec{q} = \left[\vec{x}_0; \vec{p}\right]$). By linearising the function $\vec{h}(\vec{q})$ with respect to a reference state $\vec{q}^{ref}$, and computing the observations partials (or design) matrix $\boldsymbol{H}$:

$$\boldsymbol{H} = \frac{\partial \vec{h}(\vec{q}^{ref})}{\partial \vec{q}}, \tag{9}$$

we obtain a differential correction (Montenbruck and Gill, 2000):

$$\Delta\vec{q}^{\text{lsq}} = \left(\boldsymbol{H}^T \boldsymbol{W} \boldsymbol{H}\right)^{-1} \left(\boldsymbol{H}^T \boldsymbol{W} \Delta\vec{z}\right). \tag{10}$$

By computing the above correction iteratively, we obtain a best estimate of $\vec{q}$. Here, we have introduced the weight matrix $\boldsymbol{W}$ (or observation covariance) to account for different levels of observation uncertainties. Usually, this weight matrix is set as a square diagonal matrix such that $\boldsymbol{W}_{ii} = \sigma_{h,i}^{-2}$, with $\sigma_{h,i}$ the uncertainty in entry i of $\vec{z}$, implicitly assuming all uncertainties to be uncorrelated white noise with a Gaussian distribution.

4.2. Covariance analysis

We are interested in the uncertainty of both the parameters $\vec{p}$, and the evolution of the uncertainty of the states $\vec{x}$, with the latter being obtained from propagating the uncertainty in the estimated $\vec{x}_0$. To achieve this, we will use covariance analysis, having already implicitly introduced the covariance matrix of $\vec{q}$ as the first factor of the linear least-squares solution (see Eq. (10)):

$$\boldsymbol{P}_{qq} = \left(\boldsymbol{H}^T \boldsymbol{W} \boldsymbol{H}\right)^{-1}. \tag{11}$$

To obtain the formal errors σ_j of the estimated states at a later time, the initial covariance matrix $\boldsymbol{P}_{qq}(t_0)$ can be used to compute the state covariance at any time t (*e.g.* Fayolle et al., 2022):

$$\boldsymbol{P}(t) = \left[\boldsymbol{\Phi}\left(t, t_0\right); \boldsymbol{S}(t)\right] \boldsymbol{P}(t_0) \left[\boldsymbol{\Phi}\left(t, t_0\right); \boldsymbol{S}(t)\right]^T. \tag{12}$$

The state transition and sensitivity matrix – denoted by $\boldsymbol{\Phi}\left(t, t_0\right)$ and $\boldsymbol{S}(t)$, respectively – are given by:

$$\boldsymbol{\Phi}\left(t, t_0\right) = \frac{\partial \vec{x}(t)}{\partial \vec{x}_0}; \quad \boldsymbol{S}(t) = \frac{\partial \vec{x}(t)}{\partial \vec{p}}. \tag{13}$$

Results of covariance analyses, specifically formal errors, must be treated with caution since they are known to provide an overly optimistic assessment of the real uncertainties. Only if the applied dynamical models, observational models, and noise characterisation (through the weights matrix) are a perfect representation of reality will the formal errors given by a covariance analysis be statistically representative of the true errors. Given the conceptual nature of our work, we are mainly interested in the relative contribution of space-based astrometry to the orbital solution and the overall ability of optical observations to constrain the offset between the COF and COM of Io (see Section 4.4). Therefore, a covariance analysis is suitable to our purposes, since its results for relative improvement in uncertainties will be much less sensitive to overly optimistic estimates of the *absolute* uncertainties (*e.g.* Dirkx et al., 2017).

Nevertheless, to interpret and reflect on our results, it is useful to have a reasonable idea of the range of values that the true-to-formal-error may have. For planetary ephemerides, Jones et al. (2015, 2020) estimate a true-to-formal-error ratio of about 2-3. For the estimation of Mars' gravity field and Love numbers from radio tracking data of the Mars Reconnaissance Orbiter, for instance, Konopliv et al. (2011) have found substantially larger true-to-formal-error ratios (5–20). The discrepancy between the two is likely due to the larger issues associated with the detailed dynamical modelling of spacecraft (in particular non-conservative forces) as opposed to natural bodies. In addition, the cadence of data used for planetary ephemeris general is much lower than for spacecraft orbit determination, so that in the case of the latter mismodelling (or omitting) time-correlation in noise of the data will result in an overly optimistic formal errors. Although our topic of interest is natural body dynamics (for which true-to-formal-errors are typically relatively low), we must keep in mind that the radio science solution which we use as a priori constraint determines the satellite ephemerides through their impact on spacecraft tracking (for which true-to-formal-errors are typically higher). In addition, the lack of flybys of Io by JUICE or Europa Clipper leads to a significantly imbalanced data set, with a potential destabilising effect of the true-to-formal-error ratio. This issue may be further exacerbated by the fact that, as a result of the extremely high quality of the ephemerides, also the dynamical modelling of the moons themselves, not only the spacecraft, may become a limiting factor (Fayolle et al., 2022). Altogether, these issues make it difficult to assess the range of values of true-to-formal-errors that may be expected for the ephemerides. We investigate the impact of this in Section 5.3, and further discuss how and to which extent space-based astrometry could contribute to placing constraints on large true-to-formal-errors in the radio science solution in Section 6.1.

4.3. Constraining the solution by radio science uncertainty

Usually, some information on the *a priori* accuracy of the parameters $\vec{q}$ is used to constrain the estimation. To incorporate this *a priori* covariance matrix $\boldsymbol{P}_0$, Eq. (11) can be slightly expanded and thus takes the form:

$$\boldsymbol{P} = \left(\boldsymbol{P}_0^{-1} + \boldsymbol{H}^T \boldsymbol{W} \boldsymbol{H}\right)^{-1}. \tag{14}$$

By accounting for prior knowledge of the estimated parameters, *a priori* matrices stabilise problems for which the numerical inversion of

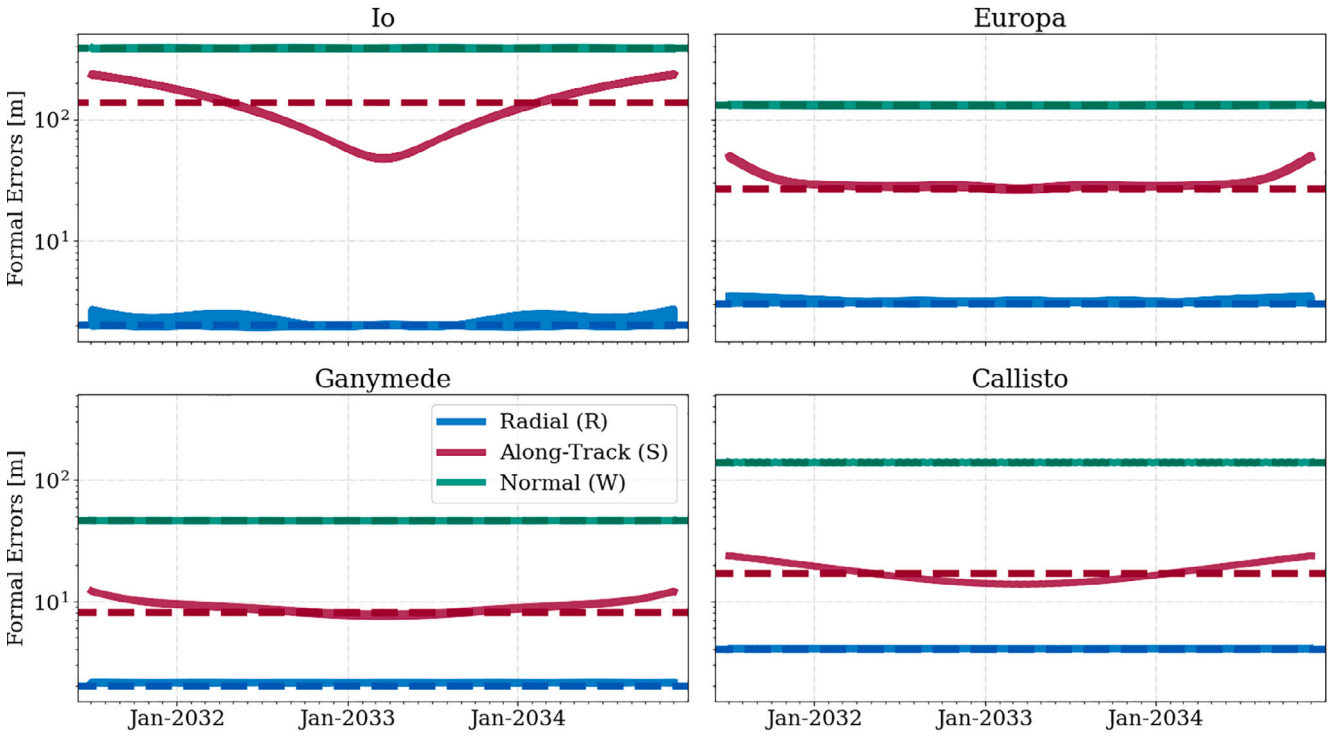

Fig. 1. Evolution of the formal *a priori* radio science uncertainties in the position of the Galilean moons over the duration of the Jovian orbital phase of JUICE. Dashed lines indicate the average values by Fayolle et al. (2023).

$\boldsymbol{H}^T\boldsymbol{W}\boldsymbol{H}$ becomes strongly ill-posed. For instance, the indirect determination of Io's ephemeris via the Laplace resonance (see Section 4.2) poses such a problem.

For our application, the nominal (*a priori*) condition is the radio science solution of the Galilean moons after the JUICE and Europa Clipper missions. To constrain our covariance analysis to the expected uncertainty, without having to perform the full radio science analysis, we will define an *a priori* covariance that mimics the resulting (average) propagated formal errors that would result from such an analysis (such as performed by Fayolle et al. 2023). To this end, we use a method similar to Lainey et al. (2007), originally used to fit the initial state of the Martian moons to their respective ephemerides.

First, we fit the initial state of the Galilean satellites to the NOE-5-2021.[4] ephemerides of the Jovian system using a 'full' estimation framework (see Section 4.1). Following Lainey et al. (2007), we treat the respective ephemeris positions as simulated observables with no assigned weights to absorb any discrepancies between the dynamical model and the ephemeris solution in the moons' initial states. Second, the same set-up – now with the updated initial states – is used to obtain the formal errors of the moons' states using a covariance analysis. While no weights were assigned to the observables within the 'full' state estimation, we have now iteratively chosen the observables' weights such that the resulting (average) propagated formal errors are almost identical to those arising from the radiometric tracking set-up by Fayolle et al. (2023). Fig. 1 visualises the propagated formal errors (obtained via Eq. (12)) of the resulting *a priori* covariance matrix.

As previously highlighted in Section 4.2, we expect the true errors of Io's radio science solution to be significantly greater. Hence, in Section 5.3, we will explicitly analyse the impact of a non-unity true-to-formal-error ratio on its ability to constrain the orbital solution of Io. Mathematically, the scaling of the formal errors σ_i and σ_j (correlated by a factor ρ_{ij}) and all associated covariance elements $\boldsymbol{P}_{ij}$ of a covariance matrix $\boldsymbol{P}(t)$ of size $n \times n$ is expressed as

$$\boldsymbol{P}(t) \rightarrow K\left[\left[\boldsymbol{\Phi}\left(t,t_0\right);\boldsymbol{S}(t)\right]\boldsymbol{P}(t_0)\left[\boldsymbol{\Phi}\left(t,t_0\right);\boldsymbol{S}(t)\right]^T\right], \tag{15a}$$

$$\boldsymbol{P}_{ij} \rightarrow \rho_{ij}\sqrt{K}\sigma_i\sqrt{K}\sigma_j = \rho_{ij}K\sigma_i\sigma_j \quad (i,j=1\ldots n), \tag{15b}$$

$$\sigma_i \rightarrow \sqrt{K}\sigma_i \quad \text{and} \quad \sigma_j \rightarrow \sqrt{K}\sigma_j. \tag{15c}$$

The constant factor K is equal to the square of the true-to-formal-error ratio, which we here assume to be equal for all relevant estimated parameters. We can further simplify the expression for a linearly scaled *a priori* covariance matrix to

$$\boldsymbol{P}(t) \rightarrow \left[\boldsymbol{\Phi}\left(t,t_0\right);\boldsymbol{S}(t)\right]\left[K\boldsymbol{P}\left(t_0\right)\right]\left[\boldsymbol{\Phi}\left(t,t_0\right);\boldsymbol{S}(t)\right]^T. \tag{16}$$

Finally, the contribution c_q of the *a priori* information to the solution of each estimated parameter will be evaluated as follows (*e.g.* Floberhagen, 2001; Fayolle et al., 2022):

$$c_q = \boldsymbol{I} - \boldsymbol{P}\boldsymbol{P}_0^{-1}, \tag{17}$$

where $\boldsymbol{I}$ is the identity matrix, while $\boldsymbol{P}$ and $\boldsymbol{P}_0$ denote the estimated and *a priori* covariance matrix. A c_q equal to nought indicates that the respective parameter's estimation is based on the provided *a priori* information, while a value of unity implies that it relies solely on the observations.

4.4. Modelling of the COF-COM-offset of Io

In general, the offset between the centre-of-figure (COF) and centre-of-mass (COM) of a celestial body can be expressed as a vector in a body-fixed frame. In this work, we will assume this vector to be constant. While the choice of the orientation of the body-fixed reference frame is entirely arbitrary, given the previously discussed geometric implications with the observability of the along-track position of Io (see Section 3.2.2), the RSW-frame has been found to be especially suitable to express the COF-COM-offset of Io. The RSW-frame is defined such that the x-axis radially points from Io to Jupiter (R), the y-axis is tangentially aligned with Io's along-track direction (S), and the z-axis

[4] https://ftp.imcce.fr/pub/ephem/satel/NOE/JUPITER/

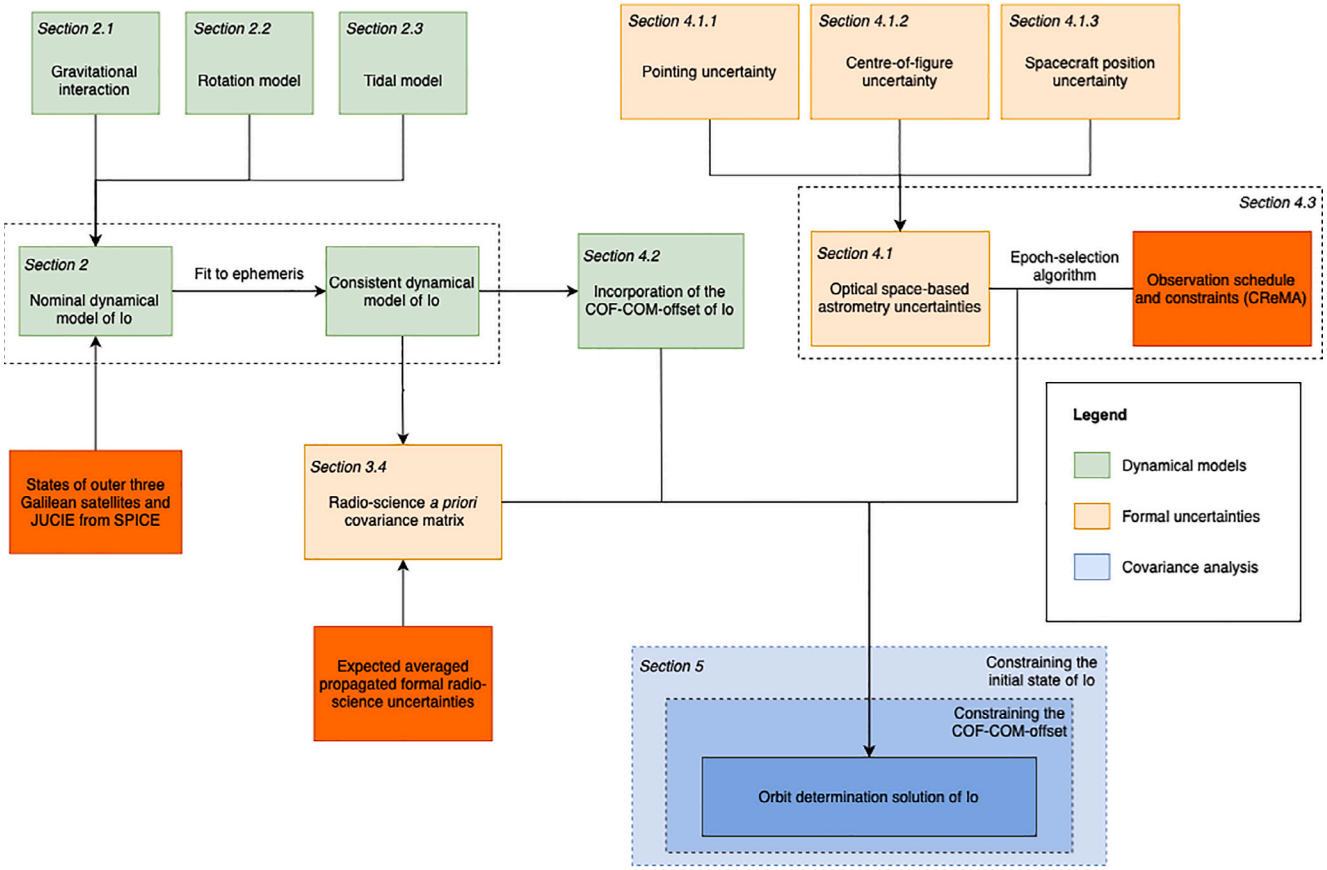

Fig. 2. Flowchart summarising the methodology followed in this work.

normally completes the reference frame (W). By definition, owing to the chosen rotation model, the RSW-frame is fixed to Io.

The COF enters our models of Io through the definition of the origin of our Io-fixed frame. If we set the origin at the COM, the non-zero offset has zero influence on the equations of motion. If we set the origin at the COF, then the offset between COF and COM enters our model as non-zero degree 1 terms in the spherical harmonic expansion of Io's gravity field ($l = 1$ in Eq. (4)), see Montenbruck and Gill (2000). We have opted to retain the standard formulation of putting Io's origin at its centre-of-mass meaning that the centre-of-figure only enters our model in the observations. Specifically, an astrometric observation of Io will provide the position of its COF, rather than its COM. This is expressed as:

$$\vec{r}(t) = \tilde{\vec{r}}_{\mathrm{Io}}(t) - \vec{r}_{\mathrm{sc}}\left(t_{\mathrm{obs}}\right) \tag{18}$$

$$\tilde{\vec{r}}_{\mathrm{Io}}(t) = \vec{r}_{\mathrm{Io}}(t) + \boldsymbol{R}(t)\,\vec{r}_{\mathrm{COF}} \tag{19}$$

where $\vec{r}$ is the position of Io's COF with respect to JUICE, from which the angles of right ascension and declination are computed. In the equations, $\tilde{\vec{r}}_{\mathrm{Io}}(t)$ and $\vec{r}_{\mathrm{Io}}(t)$ are the positions of Io's COF and COM, respectively, both being expressed in a frame with inertial orientation. The constant offset between the two in a body-fixed frame is denoted by $\vec{r}_{\mathrm{COF}}$ with $\boldsymbol{R}(t)$ the rotation matrix from Io-fixed to inertial orientation. Finally, $\vec{r}_{\mathrm{sc}}\left(t_{\mathrm{obs}}\right)$ denotes the position of JUICE, with the difference $t_{\mathrm{obs}} - t$ being equal to the observation's light-time.

Since the offset between Io's COF and COM has so far not been estimated, optical observations are implicitly treated as being taken with respect to the imaged body's COM, introducing a discrepancy between the observation and estimation model. However, by explicitly estimating the offset between the COF and COM alongside the initial state of Io, we eliminate this discrepancy, thus yielding a more realistic estimation.

In particular, we have estimated the following parameters over a single, global estimation arc:

- initial state of the Galilean moons in a jovicentric frame,
- offset between Io's COF and COM in a body-fixed frame.

Since we simulate observations of the right ascension and declination of the celestial position of Io – its COF to be precise – with respect to JUICE, to estimate the discrepancy between the COF and COM, the following partials have to be added to the design matrix (see Section 4.2):

$$\frac{\partial(\alpha,\delta)}{\partial \vec{r}_{\mathrm{COF}}} = \frac{\partial(\alpha,\delta)}{\partial \vec{r}}\,\frac{\partial \vec{r}}{\partial \vec{r}_{\mathrm{COF}}} = \frac{\partial(\alpha,\delta)}{\partial \vec{r}}\,\vec{R}(t), \tag{20}$$

where the final step follows directly from Eq. (19). Conceptually, this computation for partial derivatives is equivalent to those used for lander or ground station position estimation.

5. Results

As a brief summary of our methodology before discussing our results, all the steps of our work are highlighted in Fig. 2. We have initially delineated the different dynamical models used to propagate the moons' states (see Section 2). Subsequently, the states of all moons have been fitted to the NOE-5-2021 ephemeris in order to obtain a consistent representation of its dynamics, and we then constrained our analysis to the averaged propagated radio science formal errors – that would arise from a radiometric tracking set-up similar to the one used by Fayolle et al. (2023) – via a suitable *a priori* covariance matrix (see Section 4.3). An analytical model for the computation of the observation uncertainties associated with optical space-based astrometry has subsequently been implemented, with free parameters calibrated

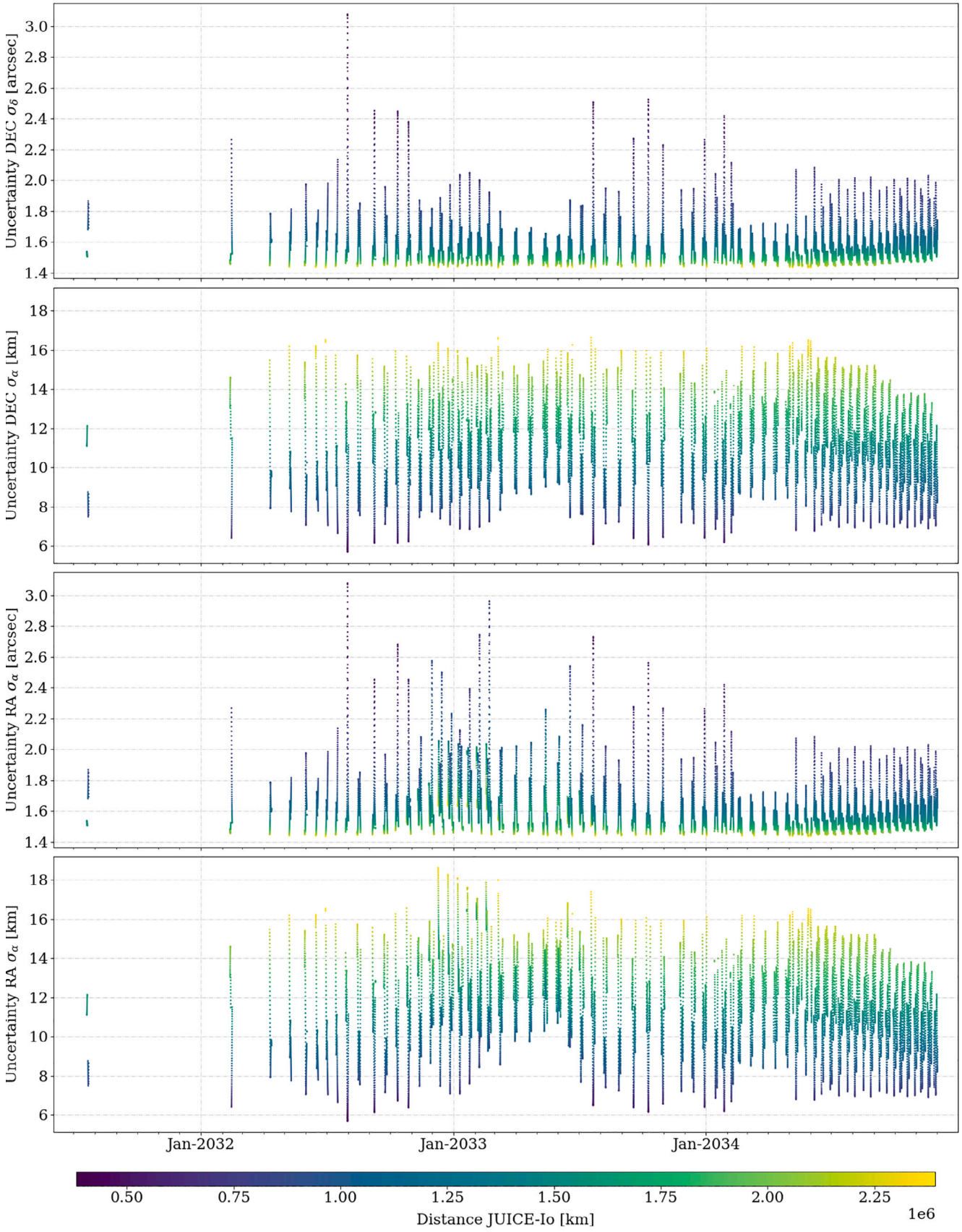

Fig. 3. Angular and linear (metric) uncertainty of space-based astrometry in right ascension (RA) and declination (DEC) for all potentially feasible epochs. Feasibility has been determined according to the previously defined viability criteria (see Section 3.2). The positions to calculate the distance between JUICE and Io have been taken from the associated SPICE kernel and the propagated orbit, respectively.

using past imagining-data obtained by Cassini (see Section 3.1). By casting these analytically evaluated uncertainties, the relative observation geometry, and the observational viability criteria into four different types of epoch selection algorithm (see Section 3.2), we have simulated optical space-based observations that are going to be used to generate the results of our covariance analyses discussed in this section.

We analyse the formal errors in the estimation of the offset between the COF and COM of Io obtained using the previously delineated methodology (see Section 4) in Section 5.2, followed by a discussion of the impact of the true-to-formal-error ratio of the *a priori* radio science solution on the estimation's overall ability to constrain the COF-COM offset and the orbital solution of Io in Section 5.3. First, however, Section 5.1 outlines the influence of different observation geometries on the quality of the obtained orbital solution.

5.1. Contributions of different observation geometries

We have defined four different algorithms for the selection of the epochs at which space-based astrometric observations are to be simulated (see Section 3.2.2). To characterise their impact on the results drivers, we first analyse the relationship between the observation geometry and the linear optical uncertainty of the selected observations in Section 5.1.1, followed by a detailed discussion of the general behaviour of the relative observation geometry in Section 5.1.2. Finally, the respective contributions in terms of linear uncertainty and observation geometry are analysed in Section 5.1.3.

5.1.1. Observation geometry – linear uncertainties

Constraining the number of potential observations only by the observation viability criteria (see Section 3.2.1) results in a total of about 15,000 feasible observation epochs. We simulate an optical data reduction pipeline using Eq. (5), yielding astrometric uncertainties visualised in Fig. 3. Overall, optical uncertainties range from a baseline of around 1.5 arcsec to slightly more than 3.0 arcsec, or approximately 6 km up to 18 km, expressed as linear position uncertainty. The expected errors are consistent with the range of values used in the simulations of JUICE space astrometry (Dirkx et al., 2017).

Fig. 3 exhibits two general trends – first, angular uncertainties increase with decreasing proximity of JUICE to Io, and second, the angular observations with the highest uncertainties correspond to the observations with the lowest linear (i.e. in terms of distance) uncertainties. Via the apparent diameter of Io, the limb-fitting uncertainty is indirectly related to the distance to JUICE – the further away one takes an image, the smaller the diameter and hence the limb-fitting error. However, as we distinctively see in Fig. 3, this is compensated for in terms of linear uncertainties by an antagonistic effect, with closer distances directly translating to lower metric errors.

5.1.2. Observation geometry – general behaviour

Besides the influence of the distance between JUICE and Io on the overall error budget, Pasewaldt et al. (2012) have highlighted that different relative observation geometries of the images being taken are crucial to constrain the offset between the COF and the COM (see Section 3.2.2). To this end, we have analysed the relative observation geometry of JUICE as seen in Io's RSW frame with each of the three subplots in Fig. 4 illustrating the observation angle with one individual axis (radial, along-track, or normal) over time. For the majority of the orbital stage of JUICE, its orbit will closely coincide with the orbital plane of the Galilean moons. The high-inclination phase of JUICE – from October 2032 to August 2033 – is the only exemption to this approximation. Thus, outside of this phase, we can treat the analysis of our problem as essentially being two-dimensional in radial and along-track direction.

Outside the high-inclination phase, no 'perfect' observations (i.e. with observation angle of 90 degrees) of the COF-COM-offset's along-track component are ever possible. The prominently centred white space in

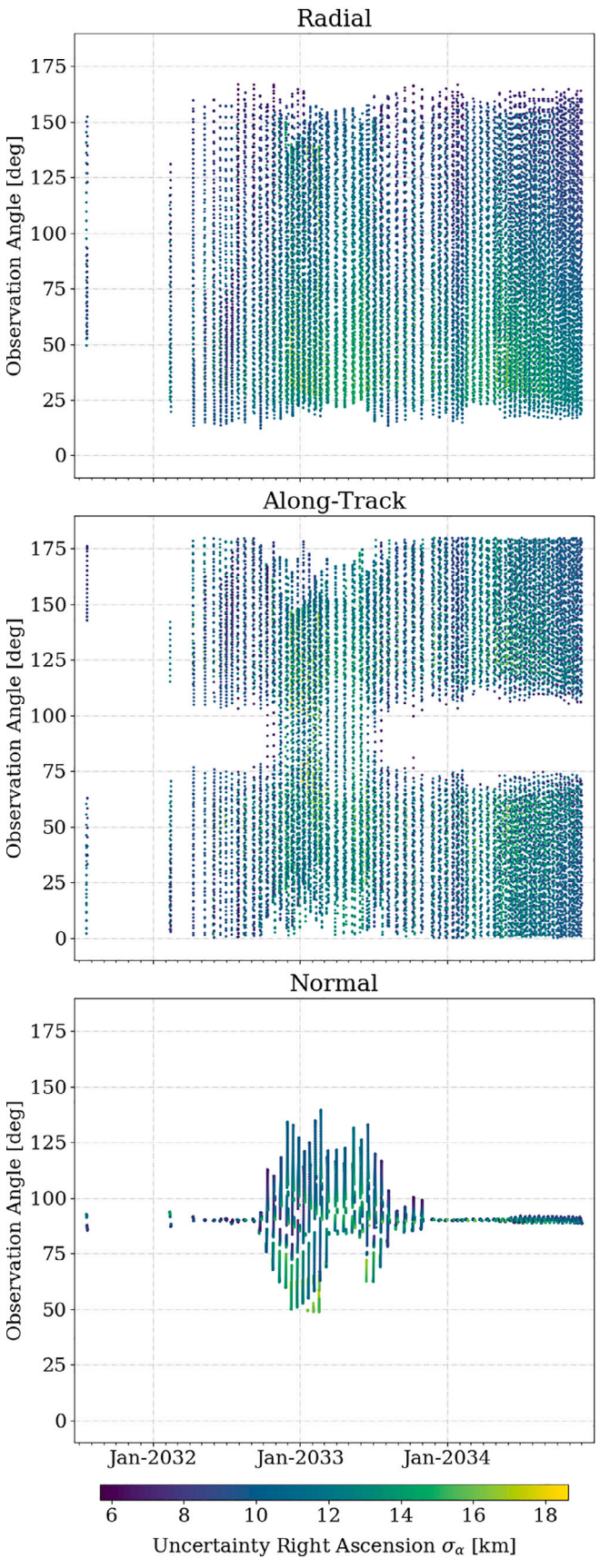

Fig. 4. Evolution of the relative observation geometry between JUICE and the body-fixed axes of Io (radial, along-track, and normal) over the duration of the Jovian orbital phase. Observations have been filtered according to the previously defined viability criteria (see Section 3.2).

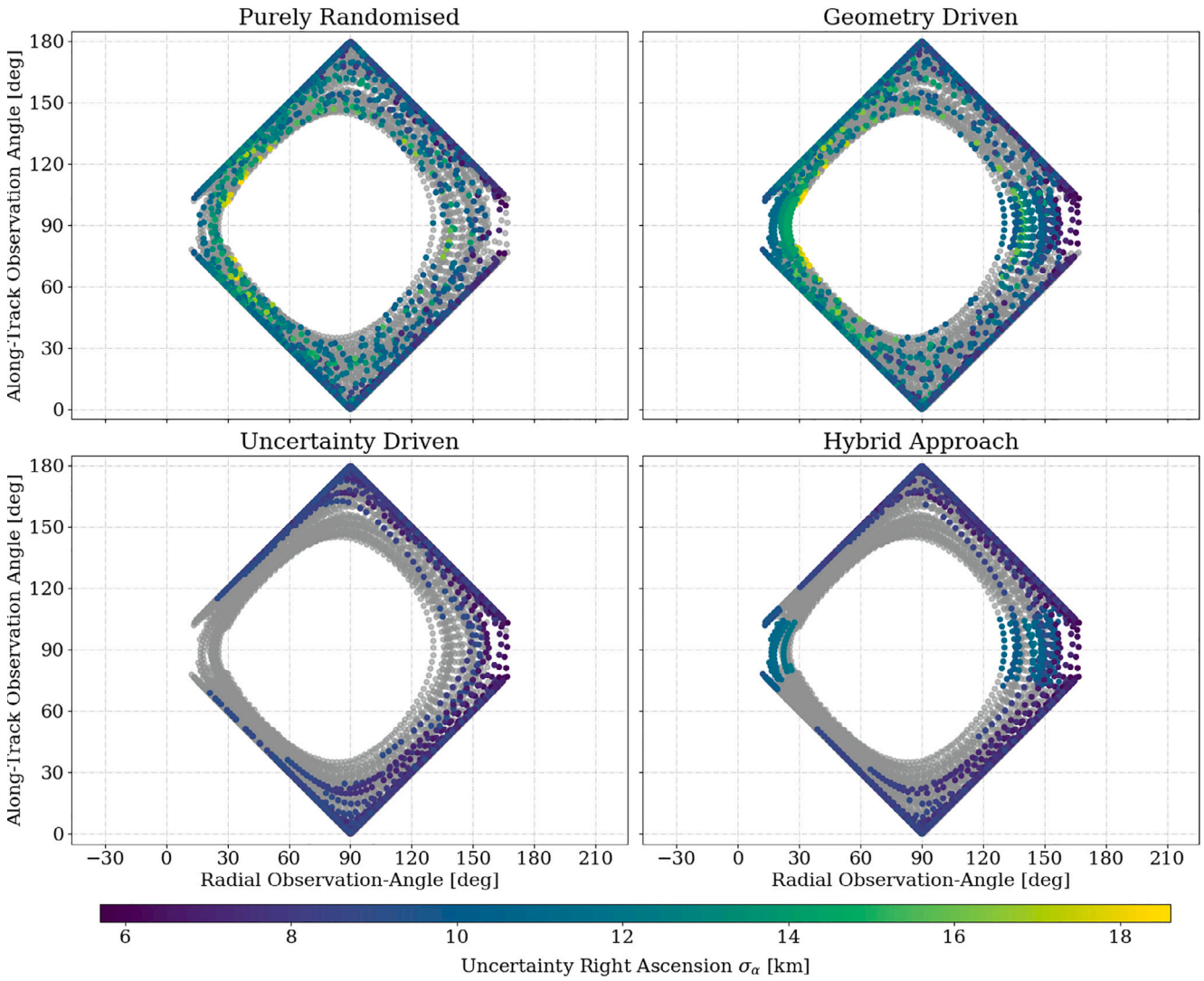

Fig. 5. Two-dimensional relative observation geometry of the radial and along-track contributions to the COF-COM-offset of Io (in grey). Each subplot exemplary illustrates the effect of the four proposed epoch-selection algorithms (see Section 3.2.2) using a total of 2560 simulated observations. Selected epochs are highlighted as a function of the respective expected uncertainty in the satellite's right ascension.

Fig. 4 rigorously underlines the lack of such observations during the planar parts of the Jovian orbital phase. This behaviour is a result of the Jupiter-Limb exclusion angle constraint (see Section 3.2), since Jupiter would be directly behind Io in the planar case. This yields a single, more poorly 'probed' component of the COF-COM-offset: the along-track direction. Only during the high-inclination phase are observations with 'perfect' observations of the along-track contribution possible. Hence, we can conclude that observations during the high-inclination phase are of particular interest, since they permit a complete range of different observation geometries.

5.1.3. Observation geometry – epoch selection algorithms

The two-dimensional relative observation geometry of the radial and along-track with respect to JUICE are provided in Fig. 5 for the four proposed epoch-selection algorithms (see Section 3.2.2) using a typical set of 2560 observations. On a general note, epochs on the edges of the square are representative of a perfectly planar observation geometry (i.e. epochs outside of the high-inclination phase). Epochs geared towards the square's centre, however, indicate the increasing three-dimensionality of the problem and thus higher inclinations.

The geometry-driven approach exhibits a clustering of observations with 90 degree along-track angle, hence during the high-inclination phase (see Section 5.1). In contrast, the uncertainty-driven method selects a significant number of epochs outside of the high-inclination phase, identifiable by the visible grouping of observations along the edges of the square. Epochs during the planar part of the Jovian orbital phase tend to have lower associated uncertainties than those during the high-inclination of JUICE. Firstly, this is due to the direct relation between the declination of observations and the respective uncertainty in right ascension (see Eq. (5)). Secondly, JUICE will perform a series of flybys around Callisto towards the end of the high-inclination phase (Grasset et al., 2013), leading to an increased mean distance – and thus smaller angular, yet greater linear errors – of JUICE with respect to Io.

The proposed hybrid approach is essentially a combination of the two previously discussed geometry and uncertainty-driven algorithms (see Section 3.2.2). This relationship is clearly reflected by Fig. 5. Owing to their favourable uncertainties, the majority of selected epochs still lie close to the edges of the square and hence during the planar parts of the Jovian orbital phase. Nonetheless, a significant number of observations is selected during the high-inclination phase. The associated observation angles are prominently centred around an observation angle with the along-track direction of 90 degrees, even though possessing a comparably higher linear uncertainty.

Finally, the uncertainty-driven and the hybrid approach highlight another distinct feature of the problem at hand – we discern a series of points seemingly trickling down from the top half of the square to the lower one. Whilst exhibiting one of the lowest uncertainties of all observations, they have a favourable observation geometry – inclined and with close proximity to Io – making these points particularly beneficial to the estimation.

5.2. Formal errors in the COF-COM-offset

To assess how well the individual approaches cope with constraining the COF-COM-offset, we analyse their respective performances in terms of achievable formal errors as a function of the total number of observations (see Fig. 6). As a first approximation, the four algorithms can be divided into two groups based on their achievable formal errors – with the random and geometry-driven methods on the one hand, and the uncertainty-driven and hybrid algorithms on the other hand, performing roughly similarly. This trend is especially pronounced for the normal direction, indicating that the relative observation geometry has a negligible effect on it, confirming our preliminary conclusion in Section 5.1. Initial improvements in the estimation of the normal COF-COM-offset between the two categories of algorithms lie around 43 per cent (from 3.35 km to 1.9 km for ten different observations), with the two categories converging to the same values for increasing numbers of observations. Yet, we can still observe improvement-ratios of approximately 21 per cent (from 290 m to 228 m) and 16 per cent (from 144 m to 121 m) for 2560 and 5120 observations, respectively.

For the two in-plane directions – radial and along-track – we find that the linear uncertainty of the individual observations remains the primary driver behind constraining the COF-COM-offset. Improvements between 30 and 50 per cent (for 10 observations), 27 and 34 per cent (for 1280 observations), and 17 and 18 per cent (for 5120 observations) in radial and along-track direction, respectively, are obtained for the two distinct groups (see Fig. 6). Within the first group, the geometry-driven approach, compared to the random selection, performs as expected – lowering the error in the along-track direction at the almost negligible expense of a minor decline in the radial uncertainty. Within the second group, the hybrid algorithm, in comparison with the uncertainty-driven approach, exhibits a slightly contrary behaviour – significantly lowering the radial error while slightly raising the along-track one for most numbers of observations. This can be explained by the presence of the previously highlighted – 'trickling' – epochs (see Fig. 5) exhibiting one of the highest accuracies whilst simultaneously having a favourable observation geometry in the chosen (uncertainty-driven) subset of observations (see Section 5.1.3). The hybrid approach, on the other hand, is designed to attain a more balanced coverage of the radial and tangential directions – having a similar observation geometry (see Fig. 5), not all of the aforementioned epochs are thus chosen by the hybrid algorithm, leading to a slight degradation of the radial error. Thus, perfectly in line with our prior conclusions, we find that optimising the observation geometry of the selected epochs leads to a more circularised uncertainty ellipse, with radial and along-track errors mutually approaching.

Concludingly, our analysis of the above-presented results has highlighted the high level of effectiveness of the hybrid approach – which will thus be chosen as exclusive epoch selection algorithm for the remaining results. We want to note that we have indirectly assumed any influence of the temporal spread of the simulated observations over the time span of the Jovian orbital phase to be entirely negligible, which has been confirmed by a preliminary analysis. Already low numbers of astrometric images (80 observations) yield low formal errors in the determination of the COF-COM-offset of about 1 kilometre – about one quarter of the number of observations required to obtain comparable uncertainties when randomly selecting epochs. Notably, for substantially higher numbers of observations, a hybrid hypothetical best-case scenario with formal uncertainties of approximately 200 metres and

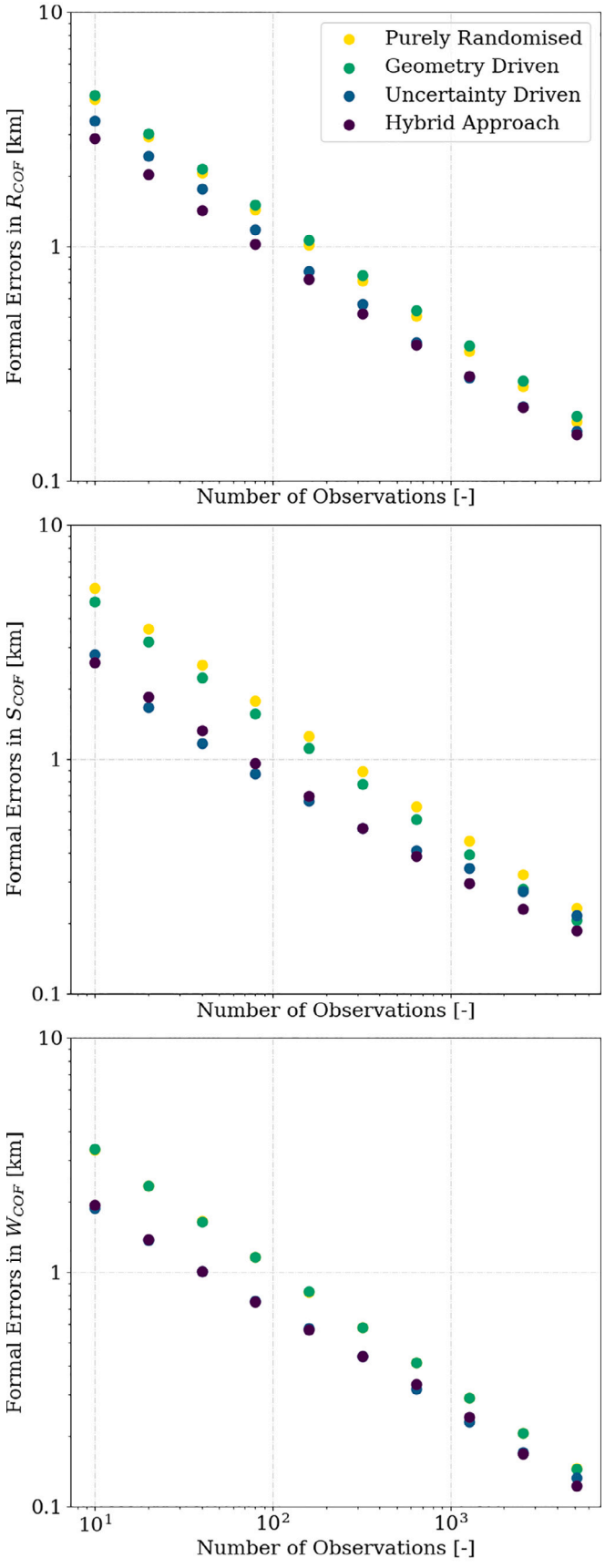

Fig. 6. Three-dimensional Monte-Carlo analysis of the formal errors in the estimation of the offset between the COF and COM for the four different selection algorithms in radial (R), along-track (S), and normal (W) direction as a function of the number of observations. Each point represents the average of 100 distinct covariance analyses.

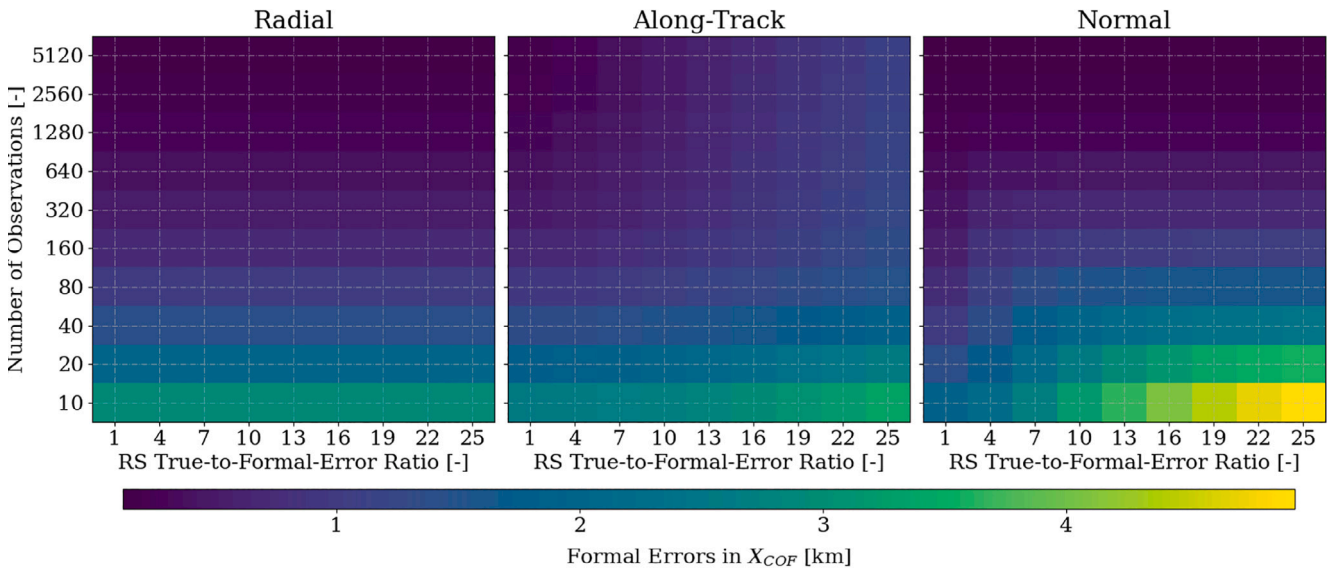

Fig. 7. Formal errors in the estimation of Io's COF-COM-offset as a function of the radio science (RS) true-to-formal-error ratio used as *a priori* information and the number of simulated observations. Each data point represents the average value of 100 distinct covariance analyses.

about 100 metres in the in-plane and out-of-plane directions, respectively, is achievable. However, less observations are to be expected. For the four regular Saturnian moons Tethys, Dione, Rhea, and Iapetus, a total of 5240 astrometric images has been taken by Cassini (Tajeddine et al., 2015), equal to an average number of 1310 observations per moon. For Io, this would translate to attainable formal uncertainties in the COF-COM-offset of no more than 300 metres.

5.3. Impact of the quality of the radio science solution

So far, our analyses have used the expected formal uncertainty levels for the Galilean moons' positions originating from a simulated joint JUICE-Europa Clipper radio science analysis. However, the true estimation errors are expected to be substantially larger than this (see Section 4.2). We investigate any effects of this by introducing a constant true-to-formal-error ratio for all four satellites' initial state elements, by linearly scaling our *a priori* covariance matrix (see Section 4.3). This scaling will have two distinct effects: firstly on the ability of the astrometric data to constrain the COF-COM-offset and secondly on the ability of the data to contribute to the determination the initial state of the Galilean moons and Io, in particular. We discuss these points in Sections 5.3.1 and 5.3.2, respectively.

5.3.1. Constraining the COF-COM-offset

The influence of variations in the radio science solution's true-to-formal-error ratio on the quality of our previous covariance analysis (see Section 5.2) as a function of the number of observations is shown in Fig. 7. With increasing true-to-formal-error ratios (i.e. a less constrained initial state) space-based astrometric observations begin to contribute to both the overall orbit determination and the estimation of the COF-COM-offset. In the correlations (see Fig. 8) we observe a related effect with increasing radio science true-to-formal-error ratios leading to stronger correlations between the initial states and the centre-of-figure offset.

For the quality of the offset's radial solution in Fig. 7, we observe that an increase in the true-to-formal-error ratio has no discernible influence, due to the extremely accurate radial orbit solution. In contrast, the along-track component is significantly affected by changes in the true-to-formal-error ratio. The influence of the number of observations is also clearly observable – as expected, with more space-based astrometry data being available, the formal errors for the COF-COM-offset in along-track direction are reduced.

For the normal component, the influence of the radio science solution's true-to-formal-error ratio is particularly significant when few space astrometry observations are available, and notably affects the estimation of the COF-COM-offset. For 20 observations, we can observe an increase in the formal error of the normal offset by a factor three when increasing the true-to-formal-error ratio from unity to 22. For more than 640 observations, however, any influence of the true-to-formal-error ratio becomes reasonably negligible. Overall, as has been the case for the along-track direction, increasing the total number of observations noticeably helps to improve the estimation of the COF-COM-offset. Nevertheless, it is interesting to note that, for large volumes of data (i.e. more than 1280 observations), the attainable uncertainty for the COF-COM-offset in the normal direction is lower than for the along-track component.

In Fig. 8, we observe increasing correlations between the along-track position of Io and the along-track contribution to the COF-COM-offset, resulting from the fact that a constant along-track orbital error and an along-track COF position error manifest themselves in the astrometric data identically (for a circular orbit). Hence, even for substantial numbers of observations, it is not possible to constrain along-track COF-COM-offset below the a priori along-track orbital error. This is distinct from the normal direction, since an initial normal position offset of Io – for instance inclination error – will lead to periodic variations in its position over time, while an initial along-track error will remain (to first-order approximation) constant.

5.3.2. Constraining the initial state of Io

In our nominal case, the orbit of Io is primarily constrained by the radio science solution, while the COF-COM-offset is constrained by optical observations. However, for increasing radio science true-to-formal-error ratios, space-based astrometry has to contribute more and more to determining the initial state of Io, in addition to its COF-COM-offset. To determine the estimation's ability to simultaneously constrain both sets of parameters, we analysed the contribution of the simulated astrometric observations to Io's orbital solution. To this end, Fig. 9 highlights the average c_q value (see Eq. (17)) of Io's position as a function of the radio science true-to-formal-error ratio and the number of observations. As expected, degrading the quality of the *a priori* radio science solution (i.e. increasing the true-to-formal-error ratio) and increasing the number of observations leads to higher c_q values, indicating that astrometric observations start contributing to Io's state estimation.

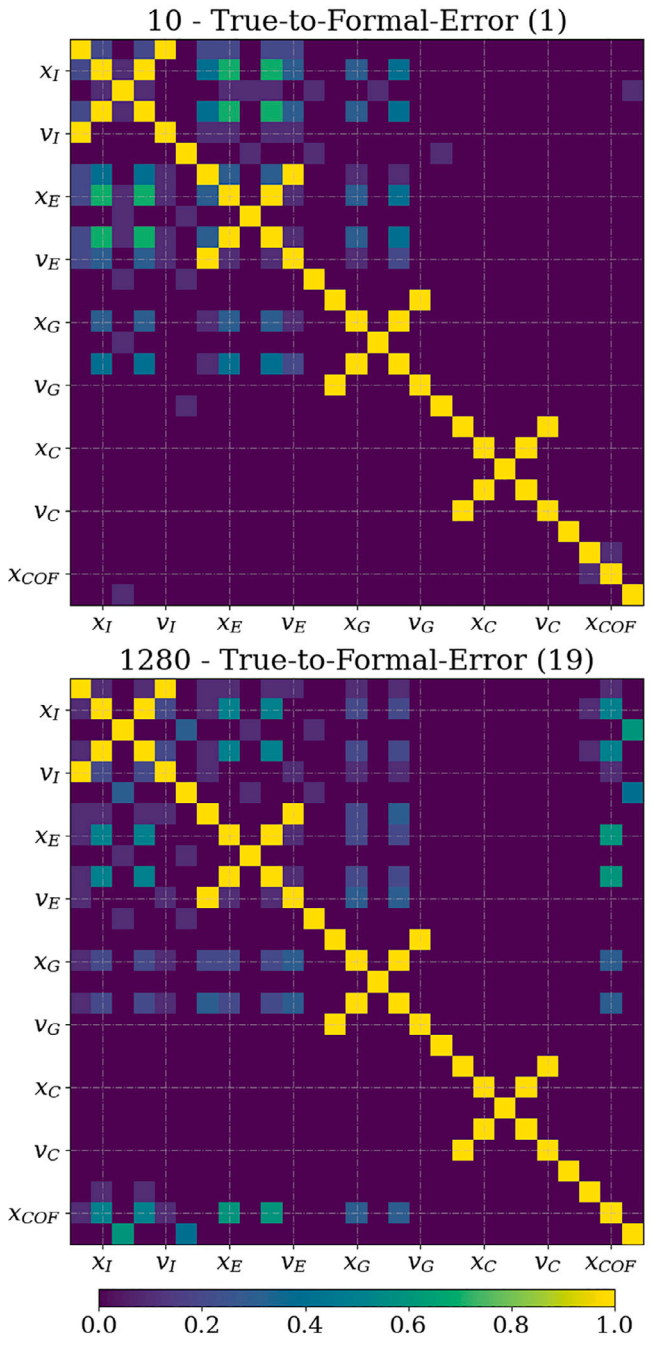

Fig. 8. Absolute correlations (indicated by the colour-bar) between the initial states of the Galilean moons and Io's COF-COM-offset expressed in body-fixed RSW-frames for 10 and 1280 observations and radio science true-to-formal-error ratios of 1 and 19, averaged for 100 different combinations of epochs.

Appreciable contributions of astrometric data to Io's state are visible in the along-track and especially the normal component – as discerned by the increasingly yellow shading in Fig. 9 towards the top-right corner of the corresponding subplots. Assuming a total number of approximately 1280 observations – based on the average number of observations taken per moon by Cassini, see Section 5.2 – minimum radio science true-to-formal-error ratios of approximately 4–7 and 1–4 for the along-track and normal direction, respectively, have been found in order for optical astrometry to have a reasonable contribution to the ephemeris estimation. For the radial position of Io, owing to the very low formal uncertainty of the *a priori* radio science solution, no significant improvements are found.

6. Discussion

Within this section, we discuss how space-based astrometric observations by JUICE would either be used to validate the radio science solution, or directly contribute to the ephemeris of Io. Subsequently, we analyse any potential insights into Io's structure that one might draw based on the offset between the COF and COM. Finally, we briefly outline how space-based observations of stellar occultations of Io might possibly supplement optical astrometry.

6.1. Validation and contribution to the orbital solution

Given the low expected formal uncertainties of the state of Io obtained by the radio science solution (see Section 4.3), the overall science return of optical space-based astrometry as stabilising contribution to the orbital solution will be more limited than it has been the case for the Saturnian moons and data obtained by Cassini (Lainey et al., 2020). Assuming a conservative number of observations (no more than approximately 200 images) as well as a moderate true-to-formal-error ratio no larger than four to seven, Fig. 9 shows that the orbital solution will in fact be entirely dominated by the radio science solution. Rather than incorporating the astrometry into the ephemeris solution, we can instead exploit the data to validate the quality (e.g. the statistical realism of the formal errors) of the *a priori* radio science solution – as discussed by Fayolle et al. (2024) for VLBI data. This validation is particularly critical for the state estimation of Io. Via the Laplace resonance, information on the orbit of Io is indeed extracted from its gravitational influence on the other Galilean satellites and is actually even more indirect in nature as it originates from its signature in the radiometric tracking data of a spacecraft, rather than in the moons' dynamics themselves. The fact that the signature of dissipation in the Jovian system will be primarily extracted from Io's orbit (Lainey et al., 2009; Van Hoolst et al., 2024) further strengthens the need for such a validation. To perform this external validation, the following procedure is followed:

- The moons' orbits are fixed to their *a priori* solution obtained from the radio tracking data.
- Subsequently, these orbits are used to computed residuals for the optical astrometry data.
- The distribution of these residuals is compared against the expected distribution obtained from the combined uncertainties of the astrometric data and the *a priori* orbit.

If the two resulting distributions – one from data and one from models – are consistent, one can place an upper bound on the true-to-formal-error ratios of the radio science ephemerides, with Fig. 9 giving an indication of the respective values. On the other hand, if astrometric residuals thus computed show a statistically significant offset from the modelled distribution, this is indicative of the true errors of the radio science solution being higher than the formal errors derived from the covariance (or, alternatively, that the astrometric data's noise and bias levels have not been properly characterised). We note that this procedure will work less effectively for validating the accuracy of the orbit in the along-track direction, since orbit error in this direction will manifest itself as almost identically to a shift in the direction of Io's centre-of-figure in its body-fixed y-direction, unless an independent upper bound (for instance from interior modelling) is placed on this component of the position of the centre-of-figure.

Instead, by combining both radio science and space-based astrometric data into a single estimation, the position of the centre-of-figure can directly be included as one of the estimated parameters alongside the initial states, dissipation parameters, *etc.* However, a significant challenge in this procedure will be the selection of suitable weights and (*a priori*) bias levels for the various data types that are fused. Our results in Fig. 9 provide direct guidance on when it may be advantageous

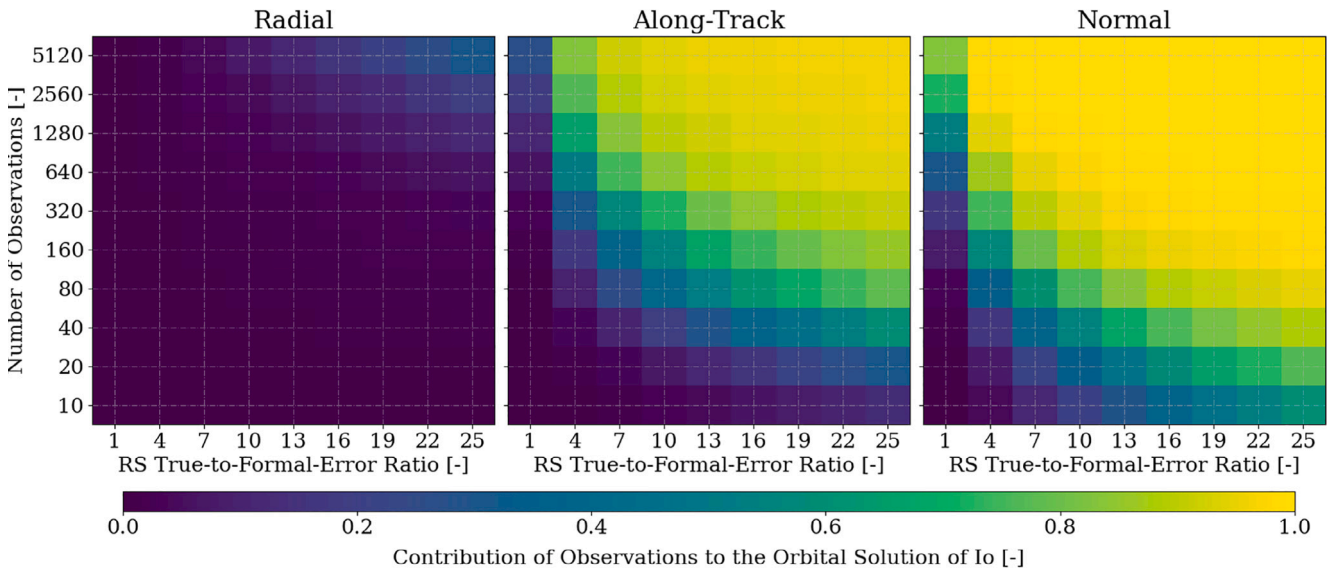

Fig. 9. Contribution of the optical space-based astrometric observations to the estimation of the initial state of Io as a function of the true-to-formal-error ratio of the radio science (RS) solution serving as *a priori* information and the number of simulated observations. Results are provided in radial (R), along-track (S), and normal (W) directions. Each data point represents the average value of 100 distinct covariance analyses.

and worth the effort to incorporate optical astrometry into such a global solution. In addition to the data considered in this work, this could include VLBI from the PRIDE experiment on JUICE (Fayolle et al., 2024), navigation data of JUICE (Hener et al., 2025), classical Earth-based astrometry (Fayolle et al., 2023), novel Earth-based optical data (Fayolle et al., 2021; Morgado et al., 2022), Earth-based radar ranging (Brozović et al., 2020) and JUICE-based stellar occultations using the ultraviolet spectrograph (Abrahams et al., 2021).

Moreover, incorporating the astrometric data into the global ephemeris solution will also allow for a (partial) validation of the radio science solution since some crucial modelling issues are avoided entirely in an astrometric data analysis. Since the astrometric data are largely insensitive to the orbit determination uncertainty of JUICE (at the relevant levels of uncertainty, see Section 3) and entirely insensitive to the data quality of the radio science solution, an increase of the true-to-formal-error ratio due to both the mismodelling of the dynamics of the spacecraft and the misweighing of the radio science data will only affect the radio science solution, but not the astrometric data.

Nonetheless, both the astrometric and radio science data analyses are sensitive to the dynamical modelling of the moons, such that part of the modelling inconsistencies may similarly impact the analysis of both data sets. However, while radio science provides highly accurate data at very specific points (during the flybys), astrometry provides much looser constraints over a more continuous time span. Hence, dynamical mismodelling of the moons will manifest itself differently in the analyses of the two data sets, possibly providing guidance on potential modelling deficiencies. In particular, one of the most critical modelling challenges in coupled JUICE-Europa Clipper radio science analyses will be the intricate feedback between the moon's orbit, tidal response, and rotation (Fayolle et al., 2022). This becomes a severe issue when extracting the moon's dynamical signature from radiometric tracking data of a spacecraft, since it requires the perfectly consistent modelling of such effects on both the orbits of the spacecraft and the moon (Fayolle, 2025), which present models cannot ensure to the required level of accuracy. This can however be easily circumvented in astrometric data analysis, where such a consistent spacecraft-moon modelling is no longer necessary.

On a final note, it has to be stressed that a quantitative definition of the cut-off values for which the contribution of the optical space-based astrometric observations to the orbital solution of Io is deemed negligible is subject to several underlying assumptions. First, the centre-of-figure, unlike the centre-of-mass, is conceptually more vaguely defined, leading to a noise floor in the contribution of the optical astrometry to the solution (at the level to which the centre-of-figure can be properly and consistently defined between observations). Second, inaccuracies in the outlined analytic simulation of image-reduction (see Section 3.1) will be a further source of uncertainty. While the first effect will only become relevant for extremely high number of observations (where the solution errors reach the level at which the COF definition becomes vague), the impact of the latter can be determined once real data is acquired and their uncertainty can be quantified.

6.2. *Constraining the interior structure of Io*

As evidenced by the values that have been found for its low-degree gravity field coefficients, Io is thought to be in hydrostatic equilibrium (Anderson et al., 2001). This conclusion is further underlined by the high level of correspondence between its observed and theoretical shape (assuming hydrostatic equilibrium), indicating a stable, balanced shape (Thomas et al., 1998). Obtainable moments of inertia thus suggest a differentiated interior structure with distinct layers – an iron core, a mantle, and a silicate crust (Van Hoolst et al., 2020). While it is commonly argued that the core of Io is molten (*e.g.* Khurana et al., 2011; Schubert et al., 2004), its radius (with estimates ranging from 650 to 950 km) and the mass fraction (respectively between 10 and 20 per cent of the total mass) hereof strongly depend on the exact (unknown) composition (Steinke, 2021). Given the observability of various mountains, the presence of a sufficiently strong lithosphere of varying thickness is assumed (Steinke et al., 2020).

So far, while no indications contradicting the presumed differentiated internal structure of Io have been observed, the state of Io's mantle remains highly questioned. In particular, the sub-layer structure and their respective thermal states are subjects of debate, with conflicting views on the mantle's melt fraction. Studies about heat convection and diffusion within the mantle suggest a melt fraction of approximately 20 per cent (Steinke et al., 2020), which is backed by the expected range of 20 to 30 per cent indicated by the eruption temperature of Io's volcanoes (Keszthelyi et al., 2007). However, Khurana et al. (2011) have argued for the presence of even more significant melt fractions or even the potential existence of a global magma ocean due to the magnetic field as measured by the Galileo probe, with high

melt fraction again having been repudiated by observations of Io's aurora (Roth et al., 2017). Recent analysis of Galileo and Juno radio science data have shown that the k_2 Love number of Io is too small to be consistent with a magma ocean (Park et al., 2024a).

Circling back to the briefly touched link between Io's interior and its tidal properties, hosting the bulk of tidal heat production, the mantle layer of Io strongly influences the interior and orbital dynamics (Steinke, 2021), yet its exact structure and composition are not fully understood. Estimations of the offset between the centre-of-figure and centre-of-mass could yield an additional constraint on both the structure and composition of Io's mantle layer, and lateral heterogeneities, in particular. Such constraints can be crucial for further narrowing down the list of compatible Io interior models. In contextualising the impact of our results, we have to distinguish two distinct cases – first, the estimated offset differs significantly from zero, or second, no statistically significant offset from zero is found. The latter was obtained for Enceladus by Park et al. (2024b), who performed a re-analysis of Cassini radiometric and optical data and obtained an uncertainty of around one kilometre in COF-COM-offset.

Any significant offset between the centre-of-figure and centre-of-mass arises from an asymmetric distribution of density in the crust or deeper interior or both, with internal heterogeneities most likely being highly dominant in producing an offset given the mass-ratio between the crust and the mantle layer. Hence, potentially hinting at the presence of anomalies in a homogeneous, symmetric density distribution due to solidified silicate, larger offsets could be an indication of a lower melt fraction in the mantle. However, by turning this argument around, any offset could also hint at the existence of an irregular pattern of regions with a higher melt fraction and temperature than surrounding areas as a result of irregular heat transfer through the mantle layer. Thus, significant offsets between the COF and COM generally suggest a more complex, asymmetric, and less homogeneous internal structure.

Given that significant variations in the conductive crust indicate changes in the crustal thickness of the order of several kilometres (Van Hoolst et al., 2020; Steinke et al., 2020), such variations would indeed lead to a certain, yet not overly significant 'baseline' COF-COM-offset (i.e. smaller than the above-assumed one, but still estimable). Assuming an otherwise symmetric distribution of density over the mantle layer, the estimation of no or an almost negligible offset would thus hint at either differences in the mineral composition – hence density – of the crust, or isostatic compensation[5] of density anomalies within the mantle by the topography. The absence of any significant COF-COM-offset is a necessary condition for the presence of a high melt fraction of silicates within Io's mantle. However, we have to stress that this is by no means a sufficient condition. In general, a small offset is thus an indication of a more homogeneous, symmetric internal structure and composition.

Finally, the quality of the estimation of the COF-COM-offset may be limited by the knowledge of Io's topography. In particular, errors in limb fitting, which will be impacted by errors in the shape model of Io used for the data reduction, will lead to variability of the actual location of the centre-of-figure for a given observation. In turn, this variability will place a lower bound on how well any COF-COM-offset can be determined and should be quantified properly when providing an error budget of the results of the proposed analysis. This issue can be partially mitigated by improved Io shape modelling from additional JUICE observations (see Section 6.3) or future missions such as the Io Volcano Observer (McEwen et al., 2014).

[5] Isostatic compensation refers to the mechanism by which any excess mass above a specific reference level (such as Earth's sea level) is countered by a deficiency in density within the underlying layers, ultimately achieving a state of isostatic equilibrium (Kearey et al., 2009).

6.3. Influence of orbital librations and tidal deformation

As roughly outlined in Section 2, the orbital eccentricity of Io leads to a time-varying gravitational torque of Jupiter, which induces a once-per-orbit libration in its rotation (Van Hoolst et al., 2020). To this end, space-based astrometry might also be sensitive to the moon's response to this combined effect. In turn, this will provide additional insights into Io's interior. In particular, the amplitude of the once-per-orbit libration in the rotation of Io not only contains information about the internal structure, but also depends on the crust's rigidity (Jara-Orué and Vermeersen, 2014; Van Hoolst et al., 2013). Depending on the adopted interior model, Van Hoolst et al. (2020) derive libration amplitudes of about 250 metres and up to approximately 1.5 kilometres without and with a magma ocean, respectively, although the latter hypothesis seems inconsistent with recent Juno results (Park et al., 2024a). In addition, the viscoelastic properties of Io's interior drive the extent to which the moon deforms under the time-varying gravitational potential exerted by Jupiter. This once-per-orbit radial deformation of Io's shape is typically quantified by its h_2 Love number, and has been shown to range from 100 to about 200 metres, again depending on Io's interior (Park et al., 2020).

We note that both the shape deformation and libration of Io will directly affect the optical astrometry by JUICE. They will indeed impact the limb fitting of Io, as well as the inertial positioning of landmarks on its surface – having a very similar effect as the topography uncertainties discussed in Section 6.2. Considering the quality of the astrometric data, as well as past experience in using astrometric data by Cassini (Lainey et al., 2019, 2023, 2024), JUICE astrometry of Io will be able to place a constraint on the moon's once-per-orbit libration, either by direct detection or by placing an upper bound on the libration amplitude as a result of a non-detection. However, the degree to which this constraint will be sufficiently stringent to provide constraints on the interior will depend on the quality and quantity of the data. The amplitude of the tidal deformation, on the other hand, is possibly too small to allow JUICE astrometry to directly determine or meaningfully constrain Io's h_2.

Synergies with other instruments on either JUICE or Europa Clipper or both may also facilitate the detection of such deformation and rotational responses. In particular, stellar occultation of Io observed using the ultraviolet spectrograph (UVS) of either mission could be timed with a precision of 1 millisecond, translating to a positioning of the in- and egress of several metres. Other sources of error might degrade this expected accuracy, since these observations will be sensitive to errors in the orbit of JUICE or to uncertainties in the topography of Io that cannot be resolved with observations by UVS. Nonetheless, such space-based occultations are still foreseen to provide invaluable constraints onto the moon's instantaneous shape, which can then be mapped to its periodic radial deformation and rotational variations. For the determination of the offset between the centre-of-figure and the centre-of-mass, the improvements in Io topography knowledge enabled by UVS data (Abrahams et al., 2021) will allow the impact of topography uncertainty on limb fitting to be reduced, thereby lowering the noise floor in the determination of the COF-COM-offset that this effect may produce. Consequently, with the addition of UVS stellar occultation data, a putative non-zero COF-COM-offset determination could more robustly be attributed to the interior, rather than the topography.

7. Conclusions

By explicitly accounting for a discrepancy between the imaged centre-of-figure and propagated centre-of-mass in the estimation process, we have introduced a method to both quantify and mitigate the offset's effect on the ephemeris estimation of Io when incorporating optical space-based astrometric observations. Given the high level of expected accuracy in Io's radio science solution (Fayolle et al., 2023;

Magnanini et al., 2024), we have discussed the extent to which astrometric imaging is able to either validate radio science of Io or constrain its state. The formal errors in Io's COF-COM-offset and the states of the Galilean moons have been estimated from simulated optical space-based astrometry as a function of the expected number of observations and the radio science true-to-formal-error ratio (see Section 5.3). We have used an analytical expression for the noise of the simulated astrometric data based on Tajeddine et al. (2015), and adapted to application for JUICE (Section 3.1). Rather than fully re-simulate the radio science solution, we have set up a priori constraints on the ephemerides as defined in Section 4.3.

Given the three-dimensional nature of the problem, variations within the relative observation geometry are crucial to the estimation of the COF-COM-offset (Pasewaldt et al., 2012). Due to the largely equatorial alignment of JUICE with respect to Io – the observation of the along-track position of Io is obstructed by the brightness of Jupiter (see Section 5.1.2), making observations taken during the high-inclination phase of JUICE of particular interest. With relative improvements between 20 and 50 per cent – compared to a purely randomised selection and depending on the number of observations, our hybrid uncertainty- and geometry-driven hybrid algorithm for the selection of epochs at which observations are to be simulated provides improved science return from the data (see Section 5.2).

We have shown that, for the discrepancy between the centre-of-figure and the centre-of-mass of Io, already low numbers of astrometric images (80 observations) yield low formal errors of about 1 kilometre – about one quarter of the number of observations required to obtain comparable uncertainties when randomly selecting epochs. A hypothetical best-case scenario (using all available observations within the estimation) with formal uncertainties of about 200 metres and 100 metres in the in-plane and out-of-plane directions, respectively, has subsequently been found. Translating Cassini's average number of 1310 observations per moon to Io, we have obtained realistically attainable formal uncertainties of no more than 300 metres.

Finally, using a Monte Carlo analysis, the expected contribution of optical observations to the combined estimation of the COF-COM-offset as well as to the ephemeris of Io as a function of the expected quality of the radio science solution and the number of astrometric observations, has been assessed (see Sections Section 5.3). We have found that, assuming a total of 1280 observations of Io, astrometry has an observable impact on Io's positional uncertainty if the radio science true-to-formal-error ratio is larger than approximately 4–7 and 1–4 for the in-plane and out-of-plane directions, respectively. Overall, it is thus likely that space-based astrometry can either contribute to, or at the very least validate, the orbital solution of Io. However, we want to underline that, as already briefly mentioned in the introduction, distant astrometric observations of Io are currently not part of the baseline operations of JUICE. Our results nonetheless highlight their potential in refining, stabilising, and validating the ephemerides solution, especially given the lack of direct constraints on the orbit of Io from radio science. We hope that these results will motivate further studies, in particular a refined quantification of the contribution of space-based imaging in a global inversion of the radio science data and space-based astrometry of both JUICE and Europa Clipper, potentially even motivating the inclusion of such observations in the overall planning of the mission.

CRediT authorship contribution statement

Kai Zenk: Writing – review & editing, Writing – original draft, Visualization, Validation, Software, Formal analysis. **Dominic Dirkx:** Writing – review & editing, Supervision, Conceptualization. **Sam Fayolle:** Writing – review & editing, Supervision, Conceptualization.

Declaration of competing interest

The authors declare that they have no known competing financial interests or personal relationships that could have appeared to influence the work reported in this paper.

Acknowledgments

The authors would like to thank the reviewers for their contributions to an improved manuscript. This research was partially funded by ESA's OSIP (Open Space Innovation Platform) program (S.F.).

Appendix. Optical space-based astrometry – validation of the centre-of-figure uncertainty for JUICE

While highly adapted reduction techniques have been developed to obtain estimates of the accuracies of space-based images (Tajeddine et al., 2013, 2015), they fall short of the description of simulated uncertainties. Thus, an analytical expression hereof is indispensable in the context of conceptual studies. However, with the only available analytical model by Antreasian et al. (2005) merely poorly agreeing with the data obtained by Cassini, we have fitted the two variable model parameters to imaging data provided by Tajeddine et al. (2015) for five Saturnian moons – Tethys, Dione, Rhea, Iapetus, and Phoebe. Fig. A.10 visualises the moon-wise results of this non-linear least-squares fit.

In general, as can be inferred from Fig. A.10, the (fitted) analytical model by Antreasian et al. (2005) is well adapted, yet the original values for the model parameters yield notable discrepancies with Cassini's data. For the four larger moons – Tethys, Dione, Rhea, and Iapetus, in particular – we obtain high levels of agreement between the fitted curves and the imaging data. Phoebe, on the other hand, has a highly irregular shape that naturally complexifies the limb-fitting process. Hence, since Cassini has furthermore taken significantly fewer images of this satellite, Phoebe's individual fit should be treated with caution. Still, to obtain a slightly conservative parameter estimate – i.e. favouring slight overestimation of the formal uncertainty over too optimistic accuracies – the slightly higher fitted parameters for Phoebe have explicitly been included in the calculation of the averaged parameters subsequently being treated as final fit. Overall, we have found values of 0.095 pixels and 0.0014 for the weighting factor $\sigma_{\min}$ and scaling factor C, respectively.

Given that the apparent diameter of the imaged moon in pixels – of which the analytical expression is a function – is a somewhat elusive quantity, we have also visualised the demeanour of the centre-of-figure uncertainty as a function of the distance between the spacecraft and the respective moon. For observations of Io by JUICE, we are especially interested in relative distances ranging from 0.04e7 to 0.25e7 kilometres, the minimum and maximum proximity for which optical space-based astrometry has been found to be possible. From Fig. A.10, we can conclude that the obtained fit within this regime is of particular quality, highlighting the high degree of the underlying potential of our fitted analytical expression.

On a final note, the artificially introduced scaling factor of $FOV_{NavCam}/FOV_{NAC} = 4/0.35$ to mimic the results that would have been expected when using a NavCam-like camera instead of Cassini's NAC needs to be addressed. Both the obtainable centre-of-figure uncertainty as well as the respective satellite's apparent diameter have to be scaled accordingly. Intuitively, while the linear scaling of the (by definition one-dimensional) apparent diameter is rather straightforward, one would expect the centre-of-figure uncertainty of the two-dimensional limb to be scaled by a scaling factor taking both dimensions of the field-of-view into account. However, owing to the limb-fitting process being performed iteratively for all horizontally interconnected lines of pixels across the satellite (for more details, see Tajeddine et al. (2013)), the respective pixel-wise information content similarly has to be scaled linearly using the above-stated scaling factor.

Data availability

Any code that is required to reproduce any data or results presented in this work is publicly available in a dedicated github-repository (https://github.com/kgzenk/juice_space_based_astrometry).

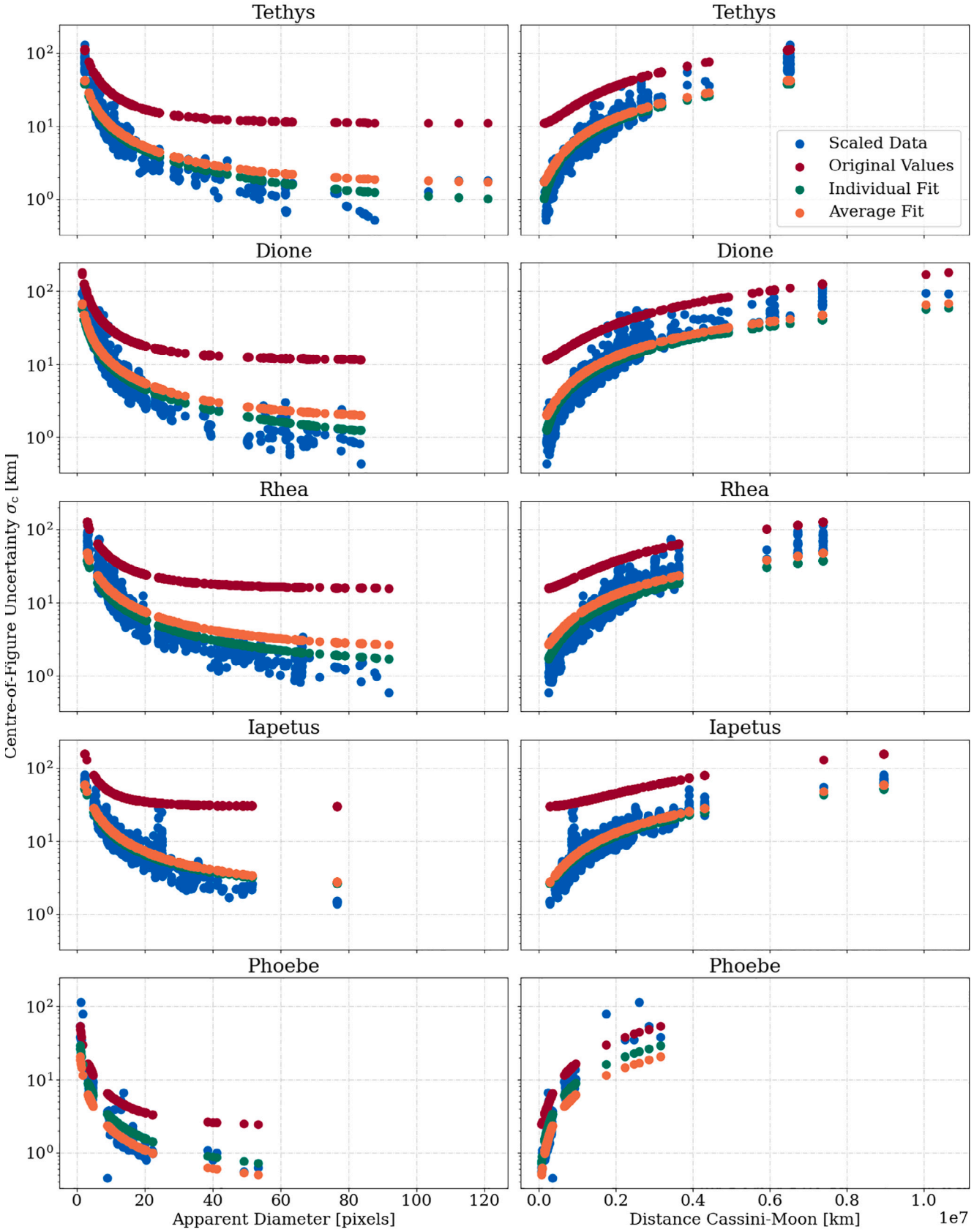

Fig. A.10. Moon-wise behaviour of both the fitted analytical model by Antreasian et al. (2005) to the data provided by Tajeddine et al. (2015) for Cassini as a function of either the apparent diameter or the distance to the respective moon. Data has been scaled to mimic the he results that would have been expected when using a NavCam-like camera instead of Cassini's NAC. Stated centre-of-figure uncertainties are thus not representative for the original accuracy achieved by Cassini, yet they demonstrate how the reduction of NavCam-like images would have performed.

References

Abrahams, J.N.H., Nimmo, F., Becker, T.M., Gladstone, G.R., Retherford, K.D., Steinbrügge, G., Mazarico, E., 2021. Improved determination of Europa's long-wavelength topography using stellar occultations. Earth Space Sci. 8 (7), http://dx.doi.org/10.1029/2020ea001586.

Anderson, J.D., Jacobson, R.A., Lau, E.L., Moore, W.B., Schubert, G., 2001. Io's gravity field and interior structure. J. Geophys. Res. Planets 106 (E12), 32963–32969. http://dx.doi.org/10.1029/2000je001367.

Antreasian, P.G., Bordi, J.J., Criddle, K.E., Ionasescu, R., Jacobson, R.A., Jones, J.B., MacKenzie, R.A., Meek, M.C., Pelletier, F.J., Roth, D.C., Roundhill, I.M., Stauch, J., 2005. Cassini orbit determination performance during the first eight orbits of the Saturn satellite tour. In: AAS/AIAA Astrodynamics Conference.

Boutonnet, A., Varga, G., Rocchi, A., Martens, W., Mackenzie, R., 2018. JUICE - Jupiter Icy moons Explorer Consolidated Report on Mission Analysis (CReMA). Report, ESA-ESOC (European Space Operations Centre).

Brozović, M., Nolan, M.C., Magri, C., Folkner, W.M., Jacobson, R.A., Harcke, L.J., McMichael, J.G., Richardson, J.E., Harmon, J.K., Taylor, P.A., et al., 2020. Arecibo radar astrometry of the Galilean satellites from 1999 to 2016. Astron. J. 159 (4), 149. http://dx.doi.org/10.3847/1538-3881/ab7023.

Cappuccio, P., Notaro, V., di Ruscio, A., Iess, L., Genova, A., Durante, D., di Stefano, I., Asmar, S.W., Ciarcia, S., Simone, L., 2020. Report on first inflight data of BepiColombo's Mercury Orbiter Radio Science Experiment. IEEE Trans. Aerosp. Electron. Syst. 56 (6), 4984–4988. http://dx.doi.org/10.1109/taes.2020.3008577.

Cooper, N.J., Murray, C.D., Lainey, V., Tajeddine, R., Evans, M.W., Williams, G.A., 2014. Cassini ISS mutual event astrometry of the mid-sized Saturnian satellites 2005–2012. Astron. Astrophys. 572, http://dx.doi.org/10.1051/0004-6361/201424555.

Cooper, N.J., Murray, C., Porco, C., Spitale, J., 2006. Cassini ISS astrometric observations of the inner Jovian satellites, Amalthea and Thebe. Icarus 181 (1), 223–234. http://dx.doi.org/10.1016/j.icarus.2005.11.007.

Davies, A.G., 2007. Volcanism on Io: A Comparison with Earth. Cambridge University Press, Cambridge, http://dx.doi.org/10.1017/cbo9781107279902.

Davies, A.G., Perry, J.E., Williams, D.A., Nelson, D.M., 2023. Io's polar volcanic thermal emission indicative of magma ocean and shallow tidal heating models. Nat. Astron. http://dx.doi.org/10.1038/s41550-023-02123-5.

Dias-Oliveira, A., Vieira-Martins, R., Assafin, M., Camargo, J.I.B., Braga-Ribas, F., da Silva Neto, D.N., Gaspar, H.S., Pires dos Santos, P.M., Domingos, R.C., Boldrin, L.A.G., Izidoro, A., Carvalho, J.P.S., Sfair, R., Sampaio, J.C., Winter, O.C., 2013. Analysis of 25 mutual eclipses and occultations between the Galilean satellites observed from Brazil in 2009. Mon. Not. R. Astron. Soc. 432 (1), 225–242. http://dx.doi.org/10.1093/mnras/stt447.

Dirkx, D., Fayolle, M., Garrett, G., Avillez, M., Cowan, K., Cowan, S., Encarnacao, J., Fortuny Lombrana, C., Gaffarel, J., Hener, J., Hu, X., van Nistelrooij, M., Oggionni, F., Plumaris, M., 2022. The open-source astrodynamics Tudatpy software – overview for planetary mission design and science analysis. In: Europlanet Science Congress 2022, Granada, Spain, 18–23 Sep 2022, EPSC2022-253. http://dx.doi.org/10.5194/epsc2022-253.

Dirkx, D., Gurvits, L.I., Lainey, V., Lari, G., Milani, A., Cimò, G., Bocanegra-Bahamon, T.M., Visser, P.N.A.M., 2017. On the contribution of PRIDE-JUICE to Jovian system ephemerides. Planet. Space Sci. 147, 14–27. http://dx.doi.org/10.1016/j.pss.2017.09.004.

Dirkx, D., Lainey, V., Gurvits, L.I., Visser, P.N.A.M., 2016. Dynamical modelling of the Galilean moons for the JUICE mission. Planet. Space Sci. 134, 82–95. http://dx.doi.org/10.1016/j.pss.2016.10.011.

Dirkx, D., Mooij, E., Root, B., 2019. Propagation and estimation of the dynamical behaviour of gravitationally interacting rigid bodies. Astrophys. Space Sci. 364 (2), 37. http://dx.doi.org/10.1007/s10509-019-3521-4.

Fayolle, S., 2025. Natural satellites ephemerides - The Galilean moons' dynamics in the JUICE-Europa Clipper era (Ph.D. thesis). Technische Universiteit Delft.

Fayolle, M.S., Dirkx, D., Cimo, G., Gurvits, L.I., Lainey, V., Visser, P.N., 2024. Contribution of PRIDE VLBI products to the joint JUICE-Europa Clipper moons' ephemerides solution. Icarus 416, 116101. http://dx.doi.org/10.1016/j.icarus.2024.116101.

Fayolle, M., Dirkx, D., Lainey, V., Gurvits, L.I., Visser, P.N.A.M., 2022. Decoupled and coupled moons' ephemerides estimation strategies application to the JUICE mission. Planet. Space Sci. 219, http://dx.doi.org/10.1016/j.pss.2022.105531.

Fayolle, M., Dirkx, D., Visser, P.N.A.M., Lainey, V., 2021. Analytical framework for mutual approximations. Astron. Astrophys. 652, http://dx.doi.org/10.1051/0004-6361/202141261.

Fayolle, M., Magnanini, A., Lainey, V., Dirkx, D., Zannoni, M., Tortora, P., 2023. Combining astrometry and JUICE – Europa Clipper radio science to improve the ephemerides of the Galilean moons. Astron. Astrophys. 677, A42. http://dx.doi.org/10.1051/0004-6361/202347065.

Floberhagen, R., 2001. The Far Side: Lunar Gravimetry into the Third Millenium (Thesis). Technische Universiteit Delft.

Folkner, W.M., Iess, L., Anderson, J.D., Asmar, S.W., Buccino, D.R., Durante, D., Feldman, M., Gomez Casajus, L., Gregnanin, M., Milani, A., Parisi, M., Park, R.S., Serra, D., Tommei, G., Tortora, P., Zannoni, M., Bolton, S.J., Connerney, J.E.P., Levin, S.M., 2017. Jupiter gravity field estimated from the first two Juno orbits. Geophys. Res. Lett. 44 (10), 4694–4700. http://dx.doi.org/10.1002/2017gl073140.

French, R.G., McGhee, C.A., Frey, M., Hock, R., Rounds, S., Jacobson, R., Verbiscer, A., 2006. Astrometry of Saturn's satellites from the Hubble Space Telescope WFPC2. Publ. Astron. Soc. Pac. 118 (840), 246–259. http://dx.doi.org/10.1086/499215.

Fuller, J., Luan, J., Quataert, E., 2016. Resonance locking as the source of rapid tidal migration in the Jupiter and Saturn moon systems. Mon. Not. R. Astron. Soc. 458 (4), 3867–3879. http://dx.doi.org/10.1093/mnras/stw609.

Gaia Collaboration, 2018. Gaia data release 2: Summary of the contents and survey properties. Astron. Astrophys. 616, A1. http://dx.doi.org/10.1051/0004-6361/201833051.

Gaia Collaboration, 2021. Gaia Early Data Release 3: Summary of the contents and survey properties. Astron. Astrophys. 649, A1. http://dx.doi.org/10.1051/0004-6361/202039657.

Gomes-Júnior, A.R., Morgado, B.E., Benedetti-Rossi, G., Boufleur, R.C., Rommel, F.L., Banda-Huarca, M.V., Kilic, Y., Braga-Ribas, F., Sicardy, B., 2022. SORA: Stellar occultation reduction and analysis. Mon. Not. R. Astron. Soc. 511 (1), 1167–1181. http://dx.doi.org/10.1093/mnras/stac032.

Grasset, O., Dougherty, M.K., Coustenis, A., Bunce, E.J., Erd, C., Titov, D., Blanc, M., Coates, A., Drossart, P., Fletcher, L.N., Hussmann, H., Jaumann, R., Krupp, N., Lebreton, J.P., Prieto-Ballesteros, O., Tortora, P., Tosi, F., Van Hoolst, T., 2013. JUpiter ICy moons Explorer (JUICE): An ESA mission to orbit Ganymede and to characterise the Jupiter system. Planet. Space Sci. 78, http://dx.doi.org/10.1016/j.pss.2012.12.002.

Greenberg, R., 2010. The icy Jovian satellites after the Galileo mission. Rep. Progr. Phys. 73 (3), http://dx.doi.org/10.1088/0034-4885/73/3/036801.

Heller, R., Marleau, G.D., Pudritz, R.E., 2015. The formation of the Galilean moons and Titan in the Grand Tack scenario. Astron. Astrophys. 579, http://dx.doi.org/10.1051/0004-6361/201526348.

Hener, J., Fayolle, S., Dirkx, D., 2025. In-mission synergy of science and navigation ephemeris products—Potential benefits for JUICE statistical delta-v expenditure and beyond. Planet. Space Sci. 255, 106017. http://dx.doi.org/10.1016/j.pss.2024.106017.

Iess, L., Folkner, W.M., Durante, D., Parisi, M., Kaspi, Y., Galanti, E., Guillot, T., Hubbard, W.B., Stevenson, D.J., Anderson, J.D., Buccino, D.R., Casajus, L.G., Milani, A., Park, R., Racioppa, P., Serra, D., Tortora, P., Zannoni, M., Cao, H., Helled, R., Lunine, J.I., Miguel, Y., Militzer, B., Wahl, S., Connerney, J.E.P., Levin, S.M., Bolton, S.J., 2018. Measurement of Jupiter's asymmetric gravity field. Nature 555 (7695), 220–222. http://dx.doi.org/10.1038/nature25776.

Jacobson, R.A., 2010. The orbits and masses of the Martian satellites and the libration of Phobos. Astron. J. 139 (2), 668. http://dx.doi.org/10.1088/0004-6256/139/2/668.

Jacobson, R.A., Haw, R.J., McElrath, T.P., Antreasian, P.G., 2000. A comprehensive orbit reconstruction for the galileo prime mission in the J2000 system. J. Astronaut. Sci. 48 (4), 495–516. http://dx.doi.org/10.1007/bf03546268.

Jara-Orué, H.M., Vermeersen, B.L., 2014. The forced libration of Europa's deformable shell and its dependence on interior parameters. Icarus 229, 31–44. http://dx.doi.org/10.1016/j.icarus.2013.10.027.

Jones, D.L., Folkner, W.M., Jacobson, R.A., Jacobs, C.S., Dhawan, V., Romney, J., Fomalont, E., 2015. Astrometry of Cassini with the VLBA to improve the Saturn ephemeris. Astron. J. 149 (1), http://dx.doi.org/10.1088/0004-6256/149/1/28.

Jones, D.L., Folkner, W.M., Jacobson, R.A., Jacobs, C.S., Romney, J., Dhawan, V., 2020. Very long baseline array astrometry of cassini: The final epochs and an improved orbit of saturn. Astron. J. 159 (2), 72. http://dx.doi.org/10.3847/1538-3881/ab5f5d.

Kearey, P., Klepeis, K.A., Vine, F.J., 2009. Global Tectonics, third ed. Wiley-Blackwell, Oxford.

Keszthelyi, L., Jaeger, W., Milazzo, M., Radebaugh, J., Davies, A.G., Mitchell, K.L., 2007. New estimates for io eruption temperatures: Implications for the interior. Icarus 192 (2), 491–502. http://dx.doi.org/10.1016/j.icarus.2007.07.008.

Khurana, K.K., Jia, X., Kivelson, M.G., Nimmo, F., Schubert, G., Russell, C.T., 2011. Evidence of a global magma ocean in Io's interior. Science 332 (6034), 1186–1189. http://dx.doi.org/10.1126/science.1201425.

Konopliv, A.S., Asmar, S.W., Folkner, W.M., Karatekin, Ö., Nunes, D.C., Smrekar, S.E., Yoder, C.F., Zuber, M.T., 2011. Mars high resolution gravity fields from MRO, Mars seasonal gravity, and other dynamical parameters. Icarus 211 (1), 401–428. http://dx.doi.org/10.1016/j.icarus.2010.10.004.

Lainey, V., Arlot, J.-E., Karatekin, Ö., Van Hoolst, T., 2009. Strong tidal dissipation in Io and Jupiter from astrometric observations. Nature 459 (7249), 957–959. http://dx.doi.org/10.1038/nature08108.

Lainey, V., Casajus, L.G., Fuller, J., Zannoni, M., Tortora, P., Cooper, N., Murray, C., Modenini, D., Park, R.S., Robert, V., Zhang, Q., 2020. Resonance locking in giant planets indicated by the rapid orbital expansion of Titan. Nat. Astron. 4 (11), 1053–1058. http://dx.doi.org/10.1038/s41550-020-1120-5.

Lainey, V., Dehant, V., Pätzold, M., 2007. First numerical ephemerides of the Martian moons. Astron. Astrophys. 465 (3), 1075–1084. http://dx.doi.org/10.1051/0004-6361:20065466.

Lainey, V., Duriez, L., Vienne, A., 2004. New accurate ephemerides for the Galilean satellites of Jupiter. Astron. Astrophys. 420 (3), 1171–1183. http://dx.doi.org/10.1051/0004-6361:20034565.

Lainey, V., Duriez, L., Vienne, A., 2006. Synthetic representation of the Galilean satellites' orbital motions from L1 ephemerides. Astron. Astrophys. 456 (2), 783–788. http://dx.doi.org/10.1051/0004-6361:20064941.

Lainey, V., Jacobson, R.A., Tajeddine, R., Cooper, N.J., Murray, C., Robert, V., Tobie, G., Guillot, T., Mathis, S., Remus, F., Desmars, J., Arlot, J.-E., De Cuyper, J.-P., Dehant, V., Pascu, D., Thuillot, W., Poncin-Lafitte, C.L., Zahn, J.-P., 2017. New constraints on Saturn's interior from Cassini astrometric data. Icarus 281, 286–296. http://dx.doi.org/10.1016/j.icarus.2016.07.014.

Lainey, V., Karatekin, Ö., Desmars, J., Charnoz, S., Arlot, J.-E., Emelyanov, N., Poncin-Lafitte, C.L., Mathis, S., Remus, F., Tobie, G., Zahn, J.-P., 2012. Strong tidal dissipation in Saturn and constraints on Enceladus' thermal state from astrometry. Astron. J. 752 (1), 14. http://dx.doi.org/10.1088/0004-637x/752/1/14.

Lainey, V., Noyelles, B., Cooper, N., Rambaux, N., Murray, C., Park, R., 2019. Interior properties of the inner saturnian moons from space astrometry data. Icarus 326, 48–62. http://dx.doi.org/10.1016/j.icarus.2019.01.026.

Lainey, V., Rambaux, N., Cooper, N., Dahoumane, R., Zhang, Q., 2023. Characterising the interior of five inner Saturnian moons using Cassini ISS data. Astron. Astrophys. 670, L25. http://dx.doi.org/10.1051/0004-6361/202244757.

Lainey, V., Rambaux, N., Tobie, G., Cooper, N., Zhang, Q., Noyelles, B., Baillié, K., 2024. A recently formed ocean inside Saturn's moon Mimas. Nature 626 (7998), 280–282. http://dx.doi.org/10.1038/s41586-023-06975-9.

Lari, G., 2018. A semi-analytical model of the Galilean satellites' dynamics. Celest. Mech. Dyn. Astron. 130 (8), http://dx.doi.org/10.1007/s10569-018-9846-4.

Liebe, C.C., 1995. Star trackers for attitude determination. IEEE Aerosp. Electron. Syst. Mag. 10 (6), 10–16. http://dx.doi.org/10.1109/62.387971.

Lieske, J.H., 1998. Galilean satellite ephemerides E5. Astron. Astrophys. Suppl. Ser. 129 (2), 205–217. http://dx.doi.org/10.1051/aas:1998182.

Magnanini, A., Zannoni, M., Casajus, L.G., Tortora, P., Lainey, V., Mazarico, E., Park, R.S., Iess, L., 2024. Joint analysis of JUICE and Europa Clipper tracking data to study the Jovian system ephemerides and dissipative parameters. Astron. Astrophys. 687, A132. http://dx.doi.org/10.1051/0004-6361/202347616.

McEwen, A., Turtle, E., Hibbard, K., Reynolds, E., Adams, E., 2014. Io volcano observer (IVO): budget travel to the outer solar system. Acta Astron. 93, 539–544. http://dx.doi.org/10.1016/j.actaastro.2012.05.028.

Melman, F., 2018. Optimizing the observation schedule of the JANUS instrument to improve the Jovian system ephemerides (Ph.D. thesis). Technical University Delft.

Milani, A., Gronchi, G., 2010. Theory of Orbit Determination. Cambridge University Press, Cambridge.

Montenbruck, O., Gill, E., 2000. Satellite Orbits: Models, Methods, and Applications. Springer Berlin Heidelberg, Berlin, Heidelberg, http://dx.doi.org/10.1007/978-3-642-58351-3.

Moore, W., Schubert, G., Anderson, J., Spencer, J., 2007. The interior of Io. In: Lopes, R.M.C., Spencer, J.R. (Eds.), Io After Galileo: A New View of Jupiter's Volcanic Moon. Springer Berlin, Berlin, pp. 89–108.

Morgado, B., Gomes-Júnior, A., Braga-Ribas, F., Vieira-Martins, R., Desmars, J., Lainey, V., D'aversa, E., Dunham, D., Moore, J., Baillié, K., et al., 2022. Milliarcsecond astrometry for the Galilean moons using stellar occultations. Astron. J. 163 (5), 240. http://dx.doi.org/10.3847/1538-3881/ac6108.

Oberst, J., Matz, K.D., Roatsch, T., Giese, B., Hoffmann, H., Duxbury, T., Neukum, G., 2006. Astrometric observations of Phobos and Deimos with the SRC on Mars Express. Astron. Astrophys. 447 (3), 1145–1151. http://dx.doi.org/10.1051/0004-6361:20053929.

Palumbo, P., Roatsch, T., Lara, L.M., Castro-Marin, J.M., Della Corte, V., Hviid, S., Jaumann, R., Michaelis, H., Patel, M.R., Portyankina, G., Schmitz, N., Amoroso, M., Mugnuolo, R., Aboudan, A., Agostini, L., Althaus, C., Álvarez, F., Bartolomei, M., Behnke, T., Bilotta, T., Colombatti, G., Colosimo, A., Coustenis, A., Cremonese, G., Crews, C., Dattolo, A., Debei, S., Denk, T., Fiethe, B., Herranz, M., Hoffmann, H., Hueso, R., Koncz, A., Jiménez-Ortega, J., Lichopoj, A., Livi, L., Llamas, X., Lopes, R., Lucchetti, A., Martinez-Navajas, I., Mazzotta Epifani, E., Mertens, V., Pajola, M., Sarti, F., Schroedter, R., Stephan, K., Tosi, F., Tubiana, C., Wendler, B., Wendler, D., Williams, D., Wolff, F., Zusi, M., Chiodini, S., Ficai Veltroni, I., Galeotti, A., García-Segura, A., Greggio, D., Holland, A.D., Kenkmann, T., Leese, M.R., Magrin, D., Michalik, H., Munari, M., Noci, G.E., Paolinetti, R., Schipani, P., Soman, M., Stefanov, K.D., Turella, A., Aharonson, O., Bell, J.F., Bertini, I., Coates, A.J., Di Achille, G., Grassi, D., Groussin, O., Gwinner, K., Haruyama, J., Hauber, E., Hiesinger, H., Langevin, Y., Lainey, V., Marchi, S., Marinangeli, L., Marzari, F., Massironi, M., Mitri, G., Mottola, S., Oberst, J., Postberg, F., Poulet, F., Preusker, F., Schmidt, J., Schneider, N.M., Simon, A., Takahashi, Y., Tirsch, D., Vincendon, M., Balme, M.R., Bettanini, C., Borin, P., Capria, M.T., Elgner, S., Esposito, F., Ferranti, L., Ferrari, S., Fornasier, S., Galluzzi, V., Giacomini, L., Guzzetta, L., Jones, G.H., Kersten, E., Ledeit, L., Martellato, E., Matz, K.-D., Mennella, V., Murray, C., Otto, K.A., Pelizzo, M.G., Penasa, L., Politi, R., Popa, C., Pozzobon, R., Prieto Ballesteros, O., Re, C., Rotundi, A., Sato, M., Schmedemann, N., Shoji, D., Simioni, E., Sindoni, G., Trauthan, F., Yair, Y., 2025. The JANUS (Jovis Amorum ac Natorum Undique Scrutator) VIS-NIR multi-band imager for the JUICE mission. Space Sci. Rev. 221 (3), http://dx.doi.org/10.1007/s11214-025-01158-6.

Park, R.S., Jacobson, R.A., Gomez Casajus, L., Nimmo, F., Ermakov, A.I., Keane, J.T., McKinnon, W.B., Stevenson, D.J., Akiba, R., Idini, B., Buccino, D.R., Magnanini, A., Parisi, M., Tortora, P., Zannoni, M., Mura, A., Durante, D., Iess, L., Connerney, J.E.P., Levin, S.M., Bolton, S.J., 2024a. Io's tidal response precludes a shallow magma ocean. Nature 638 (8049), 69–73. http://dx.doi.org/10.1038/s41586-024-08442-5.

Park, R.S., Mastrodemos, N., Jacobson, R.A., Berne, A., Vaughan, A.T., Hemingway, D., Leonard, E.J., Castillo-Rogez, J.C., Cockell, C.S., Keane, J.T., et al., 2024b. The global shape, gravity field, and libration of Enceladus. J. Geophys. Res. Planets 129 (1), e2023JE008054. http://dx.doi.org/10.1029/2023JE008054.

Park, R.S., Riedel, J.E., Ermakov, A.I., Roa, J., Castillo-Rogez, J., Davies, A.G., McEwen, A.S., Watkins, M.M., 2020. Advanced Pointing Imaging Camera (APIC) for planetary science and mission opportunities. Planet. Space Sci. 194, 105095. http://dx.doi.org/10.1016/j.pss.2020.105095.

Pasewaldt, A., Oberst, J., Willner, K., Wählisch, M., Hoffmann, H., Matz, K.D., Roatsch, T., Hussmann, H., Lupovka, V., 2012. New astrometric observations of Deimos with the SRC on Mars Express. Astron. Astrophys. 545, http://dx.doi.org/10.1051/0004-6361/201118603.

Peale, S.J., Cassen, P., Reynolds, R.T., 1979. Melting of Io by tidal dissipation. Science 203 (4383), 892–894. http://dx.doi.org/10.1126/science.203.4383.892.

Roth, L., Saur, J., Retherford, K.D., Blöcker, A., Strobel, D.F., Feldman, P.D., 2017. Constraints on io's interior from auroral spot oscillations. J. Geophys. Res. Space Phys. 122 (2), 1903–1927. http://dx.doi.org/10.1002/2016ja023701.

Samuel, H., Lognonné, P., Panning, M., Lainey, V., 2019. The rheology and thermal history of Mars revealed by the orbital evolution of Phobos. Nature 569 (7757), 523–527. http://dx.doi.org/10.1038/s41586-019-1202-7.

Schubert, G., Anderson, J.D., Spohn, T., McKinnon, W.B., 2004. Interior composition, structure and dynamics of the Galilean satellites. In: Bagenal, F., Dowling, T.E., McKinnon, W.B. (Eds.), Jupiter. The Planet, Satellites and Magnetosphere. Cambridge University Press, Cambridge, pp. 281–306.

Smith, D.E., Zuber, M.T., Neumann, G.A., Lemoine, F.G., 1997. Topography of the Moon from the Clementine lidar. J. Geophys. Res. Planets 102 (E1), 1591–1611. http://dx.doi.org/10.1029/96je02940.

Steinke, T., 2021. The Curious Case of Io - Connections Between Interior Structure, Tidal Heating and Volcanism (Ph.D. thesis). Technische Universiteit Delft.

Steinke, T., Hu, H., Höning, D., van der Wal, W., Vermeersen, B., 2020. Tidally induced lateral variations of Io's interior. Icarus 335, 113299. http://dx.doi.org/10.1016/j.icarus.2019.05.001.

Tajeddine, R., Cooper, N.J., Lainey, V., Charnoz, S., Murray, C.D., 2013. Astrometric reduction of Cassini ISS images of the Saturnian satellites Mimas and Enceladus. Astron. Astrophys. 551, http://dx.doi.org/10.1051/0004-6361/201220831.

Tajeddine, R., Lainey, V., Cooper, N.J., Murray, C.D., 2015. Cassini ISS astrometry of the Saturnian satellites: Tethys, Dione, Rhea, Iapetus, and Phoebe 2004–2012. Astron. Astrophys. 575, http://dx.doi.org/10.1051/0004-6361/201425605.

Thomas, P., Davies, M., Colvin, T., Oberst, J., Schuster, P., Neukum, G., Carr, M., McEwen, A., Schubert, G., Belton, M., 1998. The shape of io from Galileo limb measurements. Icarus 135 (1), 175–180. http://dx.doi.org/10.1006/icar.1998.5987.

Van Hoolst, T., Baland, R.-M., Trinh, A., 2013. On the librations and tides of large icy satellites. Icarus 226 (1), 299–315. http://dx.doi.org/10.1016/j.icarus.2013.05.036.

Van Hoolst, T., Baland, R.-M., Trinh, A., Yseboodt, M., Nimmo, F., 2020. The librations, tides, and interior structure of Io. J. Geophys. Res. Planets 125 (8), http://dx.doi.org/10.1029/2020je006473.

Van Hoolst, T., Tobie, G., Vallat, C., Altobelli, N., Bruzzone, L., Cao, H., Dirkx, D., Genova, A., Hussmann, H., Iess, L., et al., 2024. Geophysical characterization of the interiors of Ganymede, Callisto and Europa by ESA's JUpiter ICy moons Explorer. Space Sci. Rev. 220 (5), 1–73. http://dx.doi.org/10.1007/s11214-024-01085-y.

Vienne, A., 2008. Dynamical objectives of observation of mutual events. Planet. Space Sci. 56 (14), 1797–1803. http://dx.doi.org/10.1016/j.pss.2008.02.036.

Willner, K., Oberst, J., Wählisch, M., Matz, K.D., Hoffmann, H., Roatsch, T., Jaumann, R., Mertens, V., 2008. New astrometric observations of Phobos with the SRC on Mars Express. Astron. Astrophys. 488 (1), 361–364. http://dx.doi.org/10.1051/0004-6361:200809787.

Zuber, M.T., Smith, D.E., Lemoine, F.G., Neumann, G.A., 1994. The shape and internal structure of the Moon from the Clementine mission. Science 266 (5192), 1839–1843. http://dx.doi.org/10.1126/science.266.5192.1839.